



Spatiotemporal variability and drivers of $p\text{CO}_2$ and air–sea CO_2 fluxes in the California Current System: an eddy-resolving modeling study

G. Turi, Z. Lachkar, and N. Gruber

Environmental Physics, Institute of Biogeochemistry and Pollutant Dynamics, ETH Zürich, Zürich, Switzerland

Correspondence to: G. Turi (giuliana.turi@env.ethz.ch)

Received: 7 August 2013 – Published in Biogeosciences Discuss.: 26 August 2013

Revised: 14 December 2013 – Accepted: 31 December 2013 – Published: 6 February 2014

Abstract.

We quantify the CO_2 source/sink nature of the California Current System (CalCS) and determine the drivers and processes behind the mean and spatiotemporal variability of the partial pressure of CO_2 ($p\text{CO}_2$) in the surface ocean. To this end, we analyze eddy-resolving, climatological simulations of a coupled physical–biogeochemical oceanic model on the basis of the Regional Oceanic Modeling System (ROMS).

In the annual mean, the entire CalCS within 800 km of the coast and from $\sim 33^\circ\text{N}$ to 46°N is essentially neutral with regard to atmospheric CO_2 : the model simulates an integrated uptake flux of $-0.9 \pm 3.6 \text{ Tg C yr}^{-1}$, corresponding to an average flux density of $-0.05 \pm 0.20 \text{ mol C m}^{-2} \text{ yr}^{-1}$. This near zero flux is a consequence of an almost complete regional compensation between (i) strong outgassing in the nearshore region (first 100 km) that brings waters with high concentrations of dissolved inorganic carbon (DIC) to the surface and (ii) a weaker, but more widespread uptake flux in the offshore region due to an intense biological reduction of this DIC, driven by the nutrients that are upwelled together with the DIC.

The air–sea CO_2 fluxes vary substantially in time, both on seasonal and sub-seasonal timescales, largely driven by variations in surface ocean $p\text{CO}_2$. Most of the variability in $p\text{CO}_2$ is associated with the seasonal cycle, with the exception of the nearshore region, where sub-seasonal variations driven by mesoscale processes dominate. In the regions offshore of 100 km, changes in surface temperature are the main driver, while in the nearshore region, changes in surface temperature, as well as anomalies in DIC and alkalinity (Alk) owing to changes in circulation, biological productivity and

air–sea CO_2 fluxes dominate. The prevalence of eddy-driven variability in the nearshore 100 km leads to a complex spatiotemporal mosaic of surface ocean $p\text{CO}_2$ and air–sea CO_2 fluxes that require a substantial observational effort to determine the source/sink nature of this region reliably.

1 Introduction

The coastal ocean often has not been appropriately taken into account in global carbon budget estimates, despite the fact that the associated carbon fluxes are disproportionately large with respect to the small fraction of the global ocean area that coastal oceans occupy (e.g., Liu et al., 2000; Borges et al., 2005; Chavez et al., 2007; Liu et al., 2010; Regnier et al., 2013). Global ocean models tend to be too coarse to resolve important coastal processes and observational data are often limited in space and time (e.g., Laruelle et al., 2010). Therefore, coastal air–sea CO_2 fluxes are currently still relatively poorly quantified, with considerable regional and global uncertainties.

Coastal upwelling regions are particularly dynamic in terms of carbon cycling as they experience extreme temporal and spatial variability in carbon fluxes (e.g., Friederich et al., 2002; Cai et al., 2006; Leinweber et al., 2009; Evans et al., 2011), further adding to the uncertainty in the coastal carbon budget. As the upwelled water is rich in dissolved inorganic carbon (DIC), its partial pressure of CO_2 ($p\text{CO}_2$) is very high and can often exceed atmospheric levels, hence leading to an outgassing of CO_2 . At the same time, the upwelled nutrients stimulate phytoplankton productivity, which supports a large

fixation and export of organic carbon (e.g., Muller-Karger et al., 2005). This leads to a decrease in surface ocean $p\text{CO}_2$ and enhances the drawdown of atmospheric CO_2 (e.g., Hales et al., 2005, 2012; Chavez and Messié, 2009). These opposing mechanisms and the highly variable ocean circulation with a large amount of mesoscale variability render coastal upwelling systems extremely complex with regard to carbon cycling.

The California Current System (CalCS), one of the four major eastern boundary upwelling systems, exhibits an intricate interplay of physical and biological controls on lateral and air–sea CO_2 fluxes. On the one hand, its relatively high level of eddy activity reduces biological productivity to levels below those expected on the basis of its rate of upwelling, leading also to a reduced vertical export of fixed carbon (Gruber et al., 2011; Lachkar and Gruber, 2011). On the other hand, filaments and other meso- and submesoscale structures cause a substantial lateral export of organic carbon (Nagai et al.), thereby leading to a strong decoupling between biological production and vertical carbon export (Plattner et al., 2005).

The CalCS has been the subject of many studies investigating a variety of different aspects ranging from ecosystem vulnerability to global anthropogenic perturbations such as ocean acidification (e.g., Feely et al., 2008; Gruber et al., 2012; Hauri et al., 2013) and the emergence of areas of hypoxic oxygen concentrations (e.g., Chan et al., 2008), to more process-related topics such as the phenology of coastal upwelling (e.g., Bograd et al., 2009) and the impacts of different processes on biological production (e.g., Gruber et al., 2011; Lachkar and Gruber, 2011, 2013). However, only a few studies have so far dealt with the source/sink nature of the CalCS with regard to atmospheric CO_2 or quantified the contribution of the CalCS to the global carbon budget (Borges et al., 2005; Cai et al., 2006; Chavez et al., 2007; Hales et al., 2012).

The published studies have come to rather different conclusions with regard to whether the entire CalCS is a source or a sink of atmospheric CO_2 (see Table 1). Friederich et al. (2002) found that the area off Monterey Bay, California, switched from being a sink of roughly $-0.5 \text{ mol C m}^{-2} \text{ yr}^{-1}$ during weak upwelling years (El Niño) to outgassing CO_2 at a rate of around $1.9 \text{ mol C m}^{-2} \text{ yr}^{-1}$ during strong upwelling years (La Niña). Based on this very limited set of observations used by Friederich et al. (2002) and other studies of temperate coastal upwelling systems, Borges et al. (2005) suggested that upwelling systems from 30 to 60° N act on average as weak sources with a mean flux density of $0.11 \text{ mol C m}^{-2} \text{ yr}^{-1}$. In contrast, Cai et al. (2006) argued that midlatitude upwelling shelves (also 30 – 60° N) are sinks with a mean flux density of $-1 \text{ mol C m}^{-2} \text{ yr}^{-1}$. Hales et al. (2005), whose estimates are included in those of Cai et al. (2006), found that the Oregon coast had a particularly strong sink strength of $-7.3 \text{ mol C m}^{-2} \text{ yr}^{-1}$, based on 120 days of measurements in 2001. More recent observations from the

Oregon coast by Evans et al. (2011) support the conclusion of this region being a sink, but they also showed that the air–sea CO_2 fluxes in this area are highly variable. In particular, they found very high $p\text{CO}_2$ with values exceeding $1000 \mu\text{atm}$ in late summer to early fall, while waters in that area were almost consistently undersaturated with respect to the atmosphere in winter and spring. This led to a small annual uptake with a mean flux density of $-0.3 \pm 6.8 \text{ mol C m}^{-2} \text{ yr}^{-1}$. A similar small uptake flux was reported for the Santa Monica Bay, using a limited duration, but high frequency time series (Leinweber et al., 2009).

In the first attempt to provide a CalCS-wide estimate without relying on the extrapolation of measurements from one site to the entire region, Chavez et al. (2007) collected all available $p\text{CO}_2$ observations from the Lamont–Doherty Earth Observatory (LDEO) database, and inferred an essentially neutral CalCS with an outgassing flux density of $0.03 \text{ mol C m}^{-2} \text{ yr}^{-1}$. This corresponds to a total loss of 0.5 Tg C yr^{-1} to the atmosphere over the entire west coast of the US and extending $\sim 300 \text{ km}$ offshore (first three $1^\circ \times 1^\circ$ grid boxes). Using a large set of zonal cruises offshore of Monterey Bay, Pennington et al. (2010) confirmed the nearly balanced air–sea CO_2 budget for the central part of the CalCS, but also emphasized the existence of large onshore–offshore gradients in the fluxes, with a tendency towards outgassing in the more nearshore areas and year-round uptake offshore of $\sim 52 \text{ km}$. The sink nature in the offshore region is also supported by the LDEO surface ocean CO_2 climatology of Takahashi et al. (2009), which reports a net sink of $-0.8 \text{ mol C m}^{-2} \text{ yr}^{-1}$ for the nine $4^\circ \times 5^\circ$ grid boxes that are located roughly between 400 and 800 km offshore of the west coast of the US.

Most recently, Hales et al. (2012) refined the estimate by Chavez et al. (2007) using the same data but employing a self-organizing map approach to extrapolate the observations in time and space. For the same region, i.e. the area of the central North American Pacific continental margin (22 – 50° N , within 370 km from the coast), they came to a rather different result, i.e. a moderate sink of -14 Tg C yr^{-1} for the period from 1997 to 2005, corresponding to a flux density of $-0.66 \text{ mol C m}^{-2} \text{ yr}^{-1}$. They confirmed the strong onshore–offshore differences in $p\text{CO}_2$ and CO_2 fluxes pointed out by Pennington et al. (2010), both in terms of the annual mean and the level of variability.

While these previous studies document the direction and magnitude of the air–sea CO_2 fluxes in different locations of the CalCS and reveal their subseasonal to interannual variability, their lack of consistent geographic settings, the absence of sufficiently dense and spatially extended observational coverage and their differing temporal coverage hinders the emergence of a synthetic view of the CalCS acting as a source or a sink of atmospheric CO_2 . This provides an opportunity for numerical models to complement the observational studies as they can provide a synoptic and more complete view of the spatiotemporal variability of the air–sea

Table 1. Summary of studies contributing to air–sea CO_2 flux (F_{CO_2}) quantification in the CalCS. F_{CO_2} has been converted to flux densities for better intercomparison. Positive F_{CO_2} values indicate a source to the atmosphere, while negative values mean an uptake by the surface ocean.

| Study | Type of data | Spatial coverage | Temporal coverage | F_{CO_2} [$\text{mol C m}^{-2} \text{ yr}^{-1}$] |
|--------------------------|---|---|---|--|
| This study | Modeled | ~ 33–46° N, 0–800 km offshore | Climatological simulation, representative of 2000/2001 | -0.05 ± 0.20 ($-0.9 \pm 3.6 \text{ Tg C yr}^{-1}$) |
| Hales et al. (2012) | Neural network analysis of underway (LDEO database) | North American Pacific continental margin: 22–50° N, 0–370 km offshore | 1997–2005 | -0.66 ± 0.66 ($-14 \pm 14 \text{ Tg C yr}^{-1}$) |
| Evans et al. (2011) | Underway and mooring | Central Oregon midshelf: 44.5–44.8° N, 124.4–124.2° W | Aug 2007–May 2010 | -0.3 ± 6.8^1 |
| Pennington et al. (2010) | Underway and mooring | Central California: Monterey Bay and along CalCOFI Line 67 | 1997–2001 | -0.08 (0–20km) ² $+0.75$ (20–52km) |
| Takahashi et al. (2009) | Underway (LDEO database) | 30–46° N, 120–135° W: nine 4° × 5° grid boxes | 1970–2007, reference year 2000 | -0.8 |
| Leinweber et al. (2009) | Mooring | Southern California, S. Monica Bay: 33.1° N, 118.7° W | Aug 5–Oct 4 2002 | -0.76 |
| Chavez et al. (2007) | Underway (LDEO database) | Entire west coast of the US extending ~ 300 km offshore: first three 1° × 1° grid boxes | 1979–2004, reference year 1995 | $+0.03$ |
| Cai et al. (2006) | Underway | Midlatitude upwelling shelves: 30–60° N | Various | -1.0^3 |
| Borges et al. (2005) | Underway | Temperate coastal upwelling systems: 30–60° N | Various | $+0.11^4$ |
| Hales et al. (2005) | Underway | Oregon coast: 44–45° N | May–Aug 2001: 120 days | -7.3 |
| Friederich et al. (2002) | Underway and mooring | Central California: Monterey Bay and along CalCOFI Line 67 | Jul 1997–Jul 1998: El Niño Jul 1998–Jul 1999: La Niña | -0.3 to -0.7 (El Niño) $+1.5$ to $+2.2$ (La Niña) |

¹ $p\text{CO}_2^{\text{air}}$ is assumed constant at 392 μatm . ² Pennington et al. (2010) infer a near zero flux for the central California area (34.4–40.5° N). ³ Estimates for Northern and Central California and Oregon are based on Friederich et al. (2002) and Hales et al. (2005). ⁴ Estimates for the Californian coast are based on Friederich et al. (2002).

CO_2 fluxes. The models further offer the opportunity to investigate the processes underlying the mean fluxes and their variability in considerably greater depth than currently possible with the in situ data.

In this study, we use a series of eddy-resolving simulations from a coupled physical–biogeochemical oceanic model on the basis of the Regional Oceanic Modeling System (ROMS) to quantify (i) the climatological mean air–sea CO_2 fluxes

and their drivers, (ii) the spatiotemporal variability of these fluxes, and (iii) the key drivers and processes behind the variability of these fluxes, i.e. the drivers and processes affecting surface ocean $p\text{CO}_2$. Our study shows that although the CalCS as a whole acts on average as a very weak carbon sink with respect to the atmosphere, the air–sea CO_2 fluxes are locally large and highly variable in space and time. Furthermore, the present work highlights the funda-

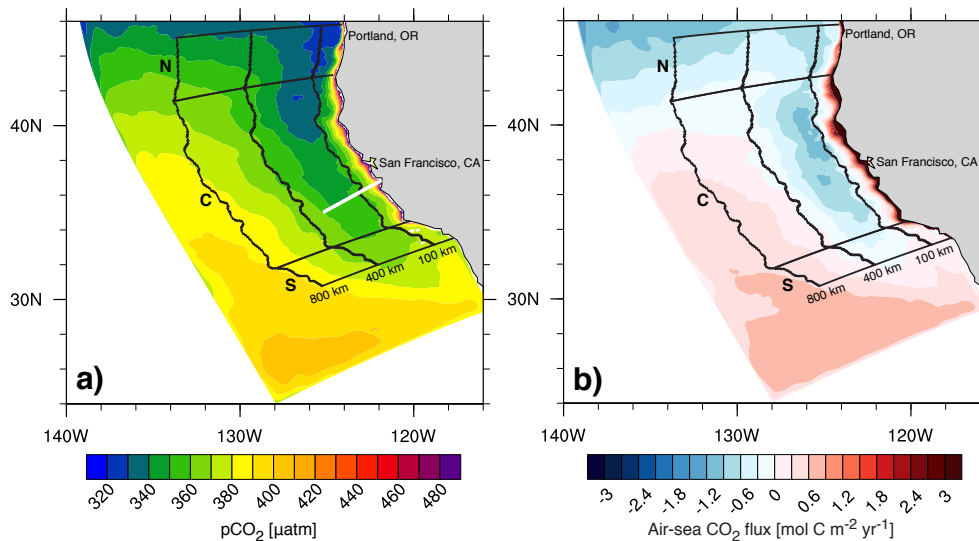


Fig. 1. Annual mean surface $p\text{CO}_2$ (a) and air–sea CO_2 flux (b) as simulated in the CalCS. Positive air–sea fluxes denote an outgassing of CO_2 . The superimposed black lines indicate the nine subdomains, where the northern (N), central (C) and southern (S) subdomains are all split into a nearshore (0–100 km), a near-offshore (100–400 km) and a far-offshore (400–800 km) subdomain. The white line in panel (a) indicates the approximate location of the MBARI/CalCOFI Line 67.

mental contrasts in the dynamics of the carbon cycle that exist between the nearshore areas dominated by the effects of upwelling and biological production and the regions further offshore where variations induced by temperature play a more prominent role. Finally, our investigation reveals that mesoscale eddies contribute substantially to surface $p\text{CO}_2$ variability in the nearshore central CalCS, making it challenging to derive a synoptic and representative view of the CO_2 fluxes on the basis of the sparse observations currently available.

2 Methods

2.1 Model details

The model used in this study is an eddy-resolving, coupled physical–biogeochemical oceanic model of the west coast of the US based on ROMS. The model domain covers roughly 2800 km alongshore (30°N – 50°N) and 1250 km offshore (Fig. 1), and has a curvilinear, coast-following grid with an average grid spacing of 5 km. The model’s vertical grid consists of 32 depth levels with increasing resolution towards the surface and in the shallower nearshore regions. The physical model is based on the UCLA-ETH version of ROMS (Marchesiello et al., 2003; Shchepetkin and McWilliams, 2005).

The biogeochemical model is a nitrogen-based nutrient–phytoplankton–zooplankton–detritus (NPZD) model and includes a single phytoplankton group, implemented to mimic diatom-like behavior. A comprehensive description of the NPZD model can be found in Gruber et al. (2006). We use

the same model setup and ecological parameters as Gruber et al. (2011).

An interactive carbon module was additionally implemented in the model and introduces three new state variables: dissolved inorganic carbon (DIC), alkalinity (Alk) and calcium carbonate (CaCO_3) (Gruber et al., 2012; Hauri et al., 2013; Lachkar and Gruber, 2013). All of these state variables are subject to physical transport and mixing, while CaCO_3 is furthermore allowed to sink at a constant rate of 20 m day^{-1} . The organic carbon cycle is linked to the organic nitrogen cycle with a fixed stoichiometric C : N ratio of 106 : 16 (Redfield et al., 1963). DIC concentrations are altered by the air–sea CO_2 flux, the precipitation and dissolution of CaCO_3 and the net community production, which is defined as net primary production (NPP) minus heterotrophic respiration. The Alk concentration is modified by the formation and removal of nitrate as well as the precipitation and dissolution of CaCO_3 . The precipitation of CaCO_3 is linked to NPP via a constant proportionality factor of 0.03, meaning that for each formed mole of organic carbon, 0.03 mol of CaCO_3 are produced. CaCO_3 dissolves at a rate of 0.0057 day^{-1} in the water column and 0.002 day^{-1} in the sediments.

We lowered the production ratio for CaCO_3 from the value of 0.07 used previously by Gruber et al. (2011) and Hauri et al. (2013) to account for the fact that their resulting CaCO_3 to organic carbon export ratio of 0.25 at 100 m depth was substantially larger than expected, while our new value of 0.09 is consistent with the global mean export ratio of about 0.06–0.11 (Lee, 2001; Sarmiento et al., 2002; Jin et al., 2006). In addition, we found that lowering the production ratio also

yielded model-simulated $p\text{CO}_2$ that compared better to observations.

The surface ocean carbonate chemistry is calculated following the standard Ocean Carbon-Cycle Model Intercomparison Project (OCMIP) carbonate chemistry routines⁵. For all our simulations, atmospheric $p\text{CO}_2$ ($p\text{CO}_2^{\text{air}}$) oscillates seasonally around a mean value of $370\ \mu\text{atm}$, which corresponds approximately to the atmospheric concentration in the years 2000 and 2001, with a seasonal amplitude of $2.9\ \mu\text{atm}$, which was taken from the NOAA Marine Boundary Layer Reference⁶ for the mean latitude of our domain.

With the partial pressures of CO_2 of atmosphere ($p\text{CO}_2^{\text{air}}$) and surface ocean ($p\text{CO}_2^{\text{sea}}$), the air–sea CO_2 flux is computed using the standard bulk formula:

$$F_{\text{CO}_2} = -K_0 \cdot k_w \cdot (p\text{CO}_2^{\text{air}} - p\text{CO}_2^{\text{sea}}), \quad (1)$$

where K_0 denotes the solubility of CO_2 , computed using the temperature- and salinity-dependent formulation of Weiss (1974), and k_w is the CO_2 gas transfer (piston) velocity. The calculation of the piston velocity for steady (short-term) winds assumes a quadratic dependence on the wind speed (Wanninkhof, 1992), using the coefficient for long-term winds. $p\text{CO}_2^{\text{sea}}$ is calculated using DIC, Alk, temperature (T), salinity (S) and nutrients, employing the first and second dissociation constants of carbonic acid of Millero (1995), with original reference to Mehrbach et al. (1973) and as refitted by Dickson and Millero (1987). Our sign convention is that positive values of F_{CO_2} denote an outgassing of CO_2 , while negative values indicate an uptake by the surface ocean.

2.2 Initial and boundary conditions

The model was started from rest and run for 12 yr with monthly climatological forcing. As our model simulations require about 5 yr for the spinup, we use model years 6–12 for analysis. For our annual mean and seasonal analyses in Sects. 3, 4, 5 and 6.1, we used model output at monthly resolution and averaged this to obtain a climatology over 7 yr. For the analysis of mesoscale processes in Sect. 6.2, we used 2-day model output and looked at all analysis years without averaging.

The initial and boundary conditions for our runs are as described in Hauri et al. (2013) and Lachkar and Gruber (2013). In particular, the DIC and Alk initial and boundary conditions were derived from the Global Ocean Data Analysis Project (GLODAP; Key et al., 2004). A seasonal cycle was added to Alk in the surface ocean, using the regression approach of Lee et al. (2006) and employing surface ocean T and S . Similarly, a seasonal cycle of surface DIC was constructed using the monthly $p\text{CO}_2$ climatology of Takahashi

Table 2. Summary of the sensitivity studies used to determine the contributions of air–sea CO_2 flux, biological production, CO_2 solubility and circulation to total $p\text{CO}_2$ from the control simulation.

| Simulation | Properties |
|-------------|--|
| CTRL | Control simulation |
| S1 | No air–sea CO_2 flux |
| S2 | No air–sea CO_2 flux, no biological production |
| S3 | No air–sea CO_2 flux, no biological production, constant CO_2 solubility |
| Calculation | Implication |
| CTRL – S1 | Contribution of air–sea CO_2 flux to total $p\text{CO}_2$ |
| S1 – S2 | Contribution of biological production to total $p\text{CO}_2$ |
| S2 – S3 | Contribution of CO_2 solubility to total $p\text{CO}_2$ |
| S3 | “Pure circulation”: $p\text{CO}_2$ if only circulation existed |

et al. (2006), and monthly surface Alk, T and S . The seasonal cycles of DIC and Alk are then modeled to penetrate into the upper thermocline, assuming that these variations are proportional to the seasonal amplitude of T at the different depths.

We slightly modified the upper ocean lateral boundary conditions of DIC inferred from GLODAP (Lee et al., 2006; Takahashi et al., 2006) in order to improve upon our model-simulated $p\text{CO}_2$, DIC and Alk fields relative to observations (see more on model evaluation in Sect. 3). The modification consisted of adjusting the vertical profile of DIC with an offset starting value of $-8\ \text{mmolCm}^{-3}$ at the surface, and then tapering off linearly with density to a depth of 350 m, below which the adjustment is zero. We determined the magnitude of this correction from the model-simulated positive DIC bias of about $10\ \text{mmolCm}^{-3}$ in the first 10 m relative to data collected from a coast-wide survey cruise undertaken from May to June 2007 by Feely et al. (2008). The most likely reason for the bias in our uncorrected boundary conditions is that they were computed from the gridded products of GLODAP and Takahashi et al. (2006), with particularly the former being based on relatively sparse observations in the eastern North Pacific. The magnitude of the correction is small relative to the uncertainties of GLODAP’s DIC gridded product, with the gridding error alone exceeding $10\ \text{mmolCm}^{-3}$ for the CalCS (Key et al., 2004).

2.3 Drivers and processes

We employ two complementary approaches to quantify and understand the causes of the spatial and temporal variability in surface ocean $p\text{CO}_2$ in Sects. 5 and 6.

In the first approach we aim to identify the role of four different drivers, namely the state variables DIC, Alk, T and S , in causing variations in $p\text{CO}_2$. To this end, we used a first-order Taylor expansion to decompose $p\text{CO}_2$ into four individual components representing the contributions from changes in these four drivers. We neglect the very small contribution arising from variations in nutrients. Following

⁵<http://ocmip5.ipsl.jussieu.fr/OCMIP/phase3/simulations/NOCES/HOWTO-NOCES-3.html>

⁶<http://www.esrl.noaa.gov/gmd/ccgg/mbl/mbl.html>

Lovenduski et al. (2007) and Doney et al. (2009), we separated the DIC and Alk changes into a part driven by freshwater (FW) fluxes and one driven by other processes, and combined the FW flux-induced changes in DIC and Alk with the changes in S to form a FW flux term, thus

$$\Delta p\text{CO}_2 \approx \underbrace{\frac{\partial p\text{CO}_2}{\partial \text{DIC}^s} \cdot \Delta \text{DIC}^s}_{\Delta p\text{CO}_2^{\text{DIC},S}} + \underbrace{\frac{\partial p\text{CO}_2}{\partial \text{Alk}^s} \cdot \Delta \text{Alk}^s}_{\Delta p\text{CO}_2^{\text{Alk},S}} + \underbrace{\frac{\partial p\text{CO}_2}{\partial T} \cdot \Delta T}_{\Delta p\text{CO}_2^T} + \underbrace{\frac{\partial p\text{CO}_2}{\partial \text{FW}} \cdot \Delta \text{FW}}_{\Delta p\text{CO}_2^{\text{FW}}}, \quad (2)$$

where DIC^s and Alk^s are the salinity-normalized concentrations of DIC and Alk (normalized to a domain mean salinity of 35), and where the partial derivatives describe the sensitivities of $p\text{CO}_2$ to small changes in DIC, Alk, T and FW (after Sarmiento and Gruber, 2006, p. 329). These partial derivatives were determined by adding a small perturbation to each driver and recalculating $p\text{CO}_2$ four times with these new values using an offline carbonate chemistry calculating tool based on the OCMIP routines. The Δ terms are the temporal or spatial anomalies from an annual or domain mean, respectively.

The second approach goes one step further by focusing on the actual processes, i.e. the processes that alter the state variables, namely the air–sea CO_2 flux, biological production, CO_2 solubility and ocean circulation. In order to identify these processes we ran a series of sensitivity studies where we consecutively removed their contributions. In addition, we ran a control simulation (CTRL) with no perturbations to be used as a reference (Table 2).

We thus separate the model-simulated $p\text{CO}_2$ of the control run ($p\text{CO}_2^{\text{Control}}$) into the following four components:

$$\underbrace{p\text{CO}_2^{\text{Control}}}_{\text{CTRL}} = \underbrace{p\text{CO}_2^{\text{Gas ex.}}}_{\text{CTRL-S1}} + \underbrace{p\text{CO}_2^{\text{Biology}}}_{\text{S1-S2}} + \underbrace{p\text{CO}_2^{\text{Solubility}}}_{\text{S2-S3}} + \underbrace{p\text{CO}_2^{\text{Circulation}}}_{\text{S3}}. \quad (3)$$

In the first sensitivity study (S1) we set the air–sea CO_2 flux coefficient in the model to zero, thereby preventing any exchange of CO_2 between the surface ocean and the atmosphere. The difference in $p\text{CO}_2$ between this simulation and the control simulation, i.e. CTRL – S1, is thus the impact of the air–sea CO_2 flux on $p\text{CO}_2$. In the second sensitivity study (S2), we started from S1, but additionally set incoming solar radiation in the model to zero, thereby inhibiting phytoplankton growth and hence eliminating biological production of organic and inorganic carbon. The difference S1 – S2 is then the impact of biological production on $p\text{CO}_2$. In the third sensitivity study (S3) we eliminated the impact of solubility, i.e. of surface ocean T and S , by setting the CO_2 solubility to a constant value. This was achieved by setting T and S within the solubility equations to domain mean values of 15 °C and 33.1, respectively. The difference S2 – S3 is then the impact of surface ocean T and S on $p\text{CO}_2$. We end up with a simulation S3, whose only remaining mechanism impacting $p\text{CO}_2$ is circulation acting upon the boundary conditions of DIC and Alk, i.e. transporting and mixing these values from the boundaries into the interior of the domain and then also to the surface, where they impact surface ocean $p\text{CO}_2$.

Due to computational resource limitation, we undertook these simulations at a slightly coarser horizontal resolution of 15 km, using the same initial conditions and running them for the same length as the full-resolution simulations. Despite the degradation in resolution, the model still manages to represent well the major mesoscale features.

In this second approach, we implicitly make the assumption that the contributions of the different processes are linearly additive. Given the nonlinearities of the ocean carbonate system (Sarmiento and Gruber, 2006), this is strictly speaking not the case. This sequential removal of processes is at best an approximate method that allows the estimation of the magnitude of each term in Eq. 3. However, our experience with a permuted sequence where we first inhibited biological production and then set the air–sea CO_2 flux to zero, showed little difference, indicating that these nonlinearities are not substantial enough to alter our results. Moreover, this kind of approach has previously been used to great effect to investigate similar questions (e.g., Murnane et al., 1999; Schmittner et al., 2013).

3 Model evaluation

A thorough model evaluation of sea surface temperature (SST), chlorophyll, mixed layer depth (MLD), density structure and NPP for the CalCS was presented by Gruber et al. (2011) and Lachkar and Gruber (2011). They found that the model reproduces the annual mean and seasonal patterns of chlorophyll and MLD reasonably well, but that the model has a cold bias of roughly 1 °C compared to satellite data. Further, Gruber et al. (2011) found an underestimation of NPP by the model of about 41 % within 1000 km and 30 % within 100 km from the coast between 34 and 42° N compared to satellite-based estimates from Kahru et al. (2009).

We extend these evaluations by comparing the model's simulated sea surface $p\text{CO}_2$ to observations from three different in situ data sources: (i) measurements of the fugacity of CO_2 ($f\text{CO}_2$) from the Surface Ocean CO_2 Atlas (SOCAT Version 2; Pfeil et al., 2013), which spans the time period from 1970 to 2011 and includes more than 220 000 observations within our model domain; (ii) $p\text{CO}_2$ measurements from the global surface $p\text{CO}_2$ (LDEO) database (Takahashi et al., 2013), spanning the period from 1957 through 2013 for our model domain and consisting of roughly 534 000 measurements; and (iii) $p\text{CO}_2$ data collected by the Naval Postgraduate School and the Monterey Bay Research Aquarium Institute (MBARI) along the California Cooperative Fisheries Investigations' (CalCOFI) Line 67 with more than 7000 data points in our domain for the years from 1997 through 2001 (Collins et al., 2003). To facilitate the comparison with the model, we first converted all data to $p\text{CO}_2$, then binned them into $0.5^\circ \times 0.5^\circ$ grid boxes and finally normalized them to the year 2000 assuming a mean annual $p\text{CO}_2$ increase rate of $1.5 \mu\text{atm yr}^{-1}$ as used by Takahashi et al. (2006,

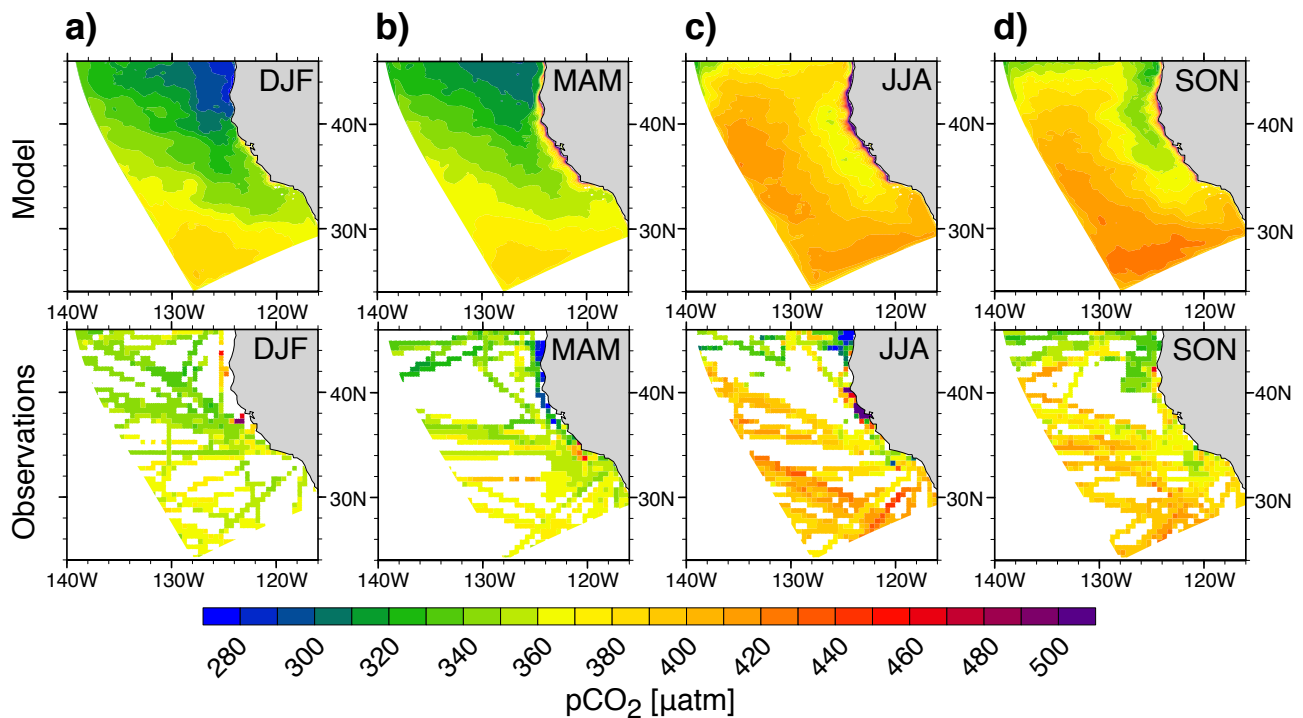


Fig. 2. Seasonally averaged modeled (upper row) and observed (lower row) surface $p\text{CO}_2$ for winter (a; DJF), spring (b; MAM), summer (c; JJA) and fall (d; SON). Observations are $p\text{CO}_2$ computed from the Surface Ocean CO_2 Atlas (SOCAT Version 2; Pfeil et al., 2013), the global surface $p\text{CO}_2$ database (Takahashi et al., 2013) and the MBARI/CalCOFI Line 67 (Collins et al., 2003). The data were first binned to $0.5^\circ \times 0.5^\circ$ grid boxes to compute a climatology, normalized to the year 2000 and then regridded to match the ROMS grid. The lower row shows all the grid boxes with observations in them, i.e. before we applied our elimination criteria.

2009). We then regridded these binned and normalized data to match our ROMS curvilinear grid and averaged $p\text{CO}_2$ over each grid box. If there were any grid boxes containing observations from different databases, we gave preference to the SOCAT database. We evaluated our model's performance for nine subdomains separately, namely a nearshore (0–100 km), a near-offshore (100–400 km) and a far-offshore (400–800 km) subdomain (see contour lines in Fig. 1). The choice of these specific subdomains is based on the magnitude and offshore extent of upwelling, as well as the distinct meridional differences in the structure of the CalCS.

Figure 2 highlights that the model has reasonable to good skills in reproducing the observed near- to offshore gradient of $p\text{CO}_2$ for all seasons, and does particularly well in the summer months when it captures the seasonal upwelling signal near the coast (Fig. 2c). The model also captures the north–south gradients and its seasonal progression, particularly in the offshore regions (Fig. 2a, b, d). However, it does have a tendency to overestimate $p\text{CO}_2$ in the nearshore regions, which is especially noticeable in the northern and central subdomains in spring and summer (Fig. 2b, c).

A more quantitative assessment of the model's successes and challenges in reproducing the observed $p\text{CO}_2$ is offered by the Taylor diagrams in Fig. 3, which provide a summary

of how well the observed and modeled $p\text{CO}_2$ patterns match in terms of their spatial correlation, their root-mean-square difference and the ratio of their standard deviations. Additionally, the diagrams show the difference between modeled and observed $p\text{CO}_2$ as a color-coded bias. For this analysis, we used only those data that fulfilled the following criteria: (i) for the annual mean analysis, only grid boxes containing at least two observations from opposite seasons were considered (i.e. DJF/JJA or MAM/SON) and (ii) for the seasonal analysis, only grid boxes with two observations taken in two different months within a season were retained. This reduced the number of grid boxes considerably, particularly in the nearshore region in winter and spring and offshore of 100 km. For the annual mean analysis, the number of available grid boxes is reduced by about 27% to a total of 38 477 grid boxes with averaged $p\text{CO}_2$ observations in them.

The annual mean correlations of the spatial pattern range between about 0.3 and 0.7 and are therefore slightly lower than the values achieved for chlorophyll (Lachkar and Gruber, 2011). Furthermore, the overall poorer performance of the model with regard to the seasonal cycle is reminiscent of the generally lower seasonal correlations found for chlorophyll, SST and mixed layer depth. However, while the variability of chlorophyll is underestimated everywhere, the

Table 3. Regional variability of annual mean surface $p\text{CO}_2$ and air–sea CO_2 fluxes in the CalCS. The $p\text{CO}_2$ difference in the last column is $p\text{CO}_2$ from our study minus $p\text{CO}_2$ from Hales et al. (2012).

| Domain | Surface area [km ²] | Air–sea CO_2 flux density [molC m ⁻² yr ⁻¹] | Integrated air–sea CO_2 flux [TgC yr ⁻¹] | $p\text{CO}_2$ [μatm] | $p\text{CO}_2$ difference to Hales et al. (2012) [μatm] |
|---------------|------------------------------------|--|--|---------------------------------------|---|
| Nearshore | | | | | |
| north | 33 781 | +0.01 | <0.01 | 350.7 | 33.6 |
| central | 112 973 | +1.11 | +1.5 | 385.2 | 3.3 |
| south | 21 681 | +0.26 | +0.1 | 366.5 | 25.4 |
| total | 168 435 | +0.78 | +1.6 | 375.9 | 11.6 |
| Near-offshore | | | | | |
| north | 108 403 | −0.49 | −0.6 | 338.0 | 3.2 |
| central | 351 808 | −0.53 | −2.2 | 349.2 | −8.4 |
| south | 65 365 | −0.15 | −0.1 | 365.0 | 4.9 |
| total | 525 576 | −0.47 | −3.0 | 348.9 | −4.3 |
| Far-offshore | | | | | |
| north | 174 720 | −0.53 | −1.1 | 352.7 | n/a |
| central | 531 430 | +0.19 | +1.2 | 374.7 | n/a |
| south | 92 230 | +0.36 | +0.4 | 381.3 | n/a |
| total | 798 380 | +0.05 | +0.5 | 370.6 | n/a |
| CalCS total | 1 492 391 | −0.05 ± 0.20 | −0.9 ± 3.6 | 363.5 | n/a |

model captures it fairly well for $p\text{CO}_2$: normalized standard deviations for all regions range between 0.4 and 2.0 with annual means of 0.6 for the nearshore region (Fig. 3c) and around 0.8 for the offshore regions (Fig. 3a, b). There exist substantial seasonal differences in the degree to which the spatial variability is captured: while the model underestimates the $p\text{CO}_2$ variability in the offshore regions in three out of four seasons, it overestimates it in spring and fall in the nearshore region.

Furthermore, the Taylor diagrams in Fig. 3 reveal substantial regional and temporal differences in the magnitude of the bias in surface ocean $p\text{CO}_2$. The magnitude of over- and underestimation is on average largest in the nearshore 0–100 km with values ranging between $-22 \mu\text{atm}$ for winter and $43 \mu\text{atm}$ for summer. Between 100 and 400 km offshore, the bias varies between $-24 \mu\text{atm}$ in winter and $14 \mu\text{atm}$ in summer. Similarly in the 400–800 km offshore region, the biases range between $-13 \mu\text{atm}$ for spring and $14 \mu\text{atm}$ for fall. In the annual mean, the model has a $p\text{CO}_2$ bias of $7 \mu\text{atm}$ in the nearshore subdomain, and biases of -6 and $4 \mu\text{atm}$ in the near- and far-offshore subdomains, respectively.

The comparison of our model to the ungridded $p\text{CO}_2$ data from CalCOFI Line 67 (Fig. 4), provides us with more detailed information about our model's performance in simulating the onshore–offshore gradient. In accordance with our results for the whole domain, the model mean $p\text{CO}_2$ of each season has a positive bias with respect to the mean observed $p\text{CO}_2$ in the first 100 km, where the model overestimates

$p\text{CO}_2$ by up to $300 \mu\text{atm}$ (summer), but on average agrees very well with the data offshore of 100 km. For all four seasons, the maximum value of modeled $p\text{CO}_2$ peaks closer to the coast than the observed $p\text{CO}_2$, i.e. in the first 10–20 km, and decreases with increasing distance to the coast. The observed $p\text{CO}_2$ reaches a maximum, on average, between 20 and 50 km offshore.

To further check the model's performance, we compared our modeled surface ocean $p\text{CO}_2$ to $p\text{CO}_2$ data predicted by the neural network model of Hales et al. (2012) (Table 3). As this data was pregridded at $0.25^\circ \times 0.25^\circ$, we regridded it to match our ROMS grid. Furthermore, we compared $p\text{CO}_2$ only for the 6 subdomains within 400 km of the coast, as the Hales et al. (2012) data extend only to about 370 km offshore. The results confirm that in the annual mean, our model consistently overestimates $p\text{CO}_2$ in the first 100 km, while between 100 and 400 km, the $p\text{CO}_2$ difference is almost negligible, with a slight underestimation by our model. This is consistent with our model evaluation with the SOCAT, LDEO and MBARI data for our whole analysis domain (Fig. 3). Over all of these six subdomains however, the model has a nearly negligible $p\text{CO}_2$ bias of $-0.3 \mu\text{atm}$ compared to data from Hales et al. (2012) (not listed in Table 3).

In conclusion, our model has very good skills in modeling the domain-wide mean $p\text{CO}_2$ and captures the observed spatial and temporal variability of $p\text{CO}_2$ well. In particular, our regional model, although benefiting from the additional constraints provided by the lateral boundary conditions, tends

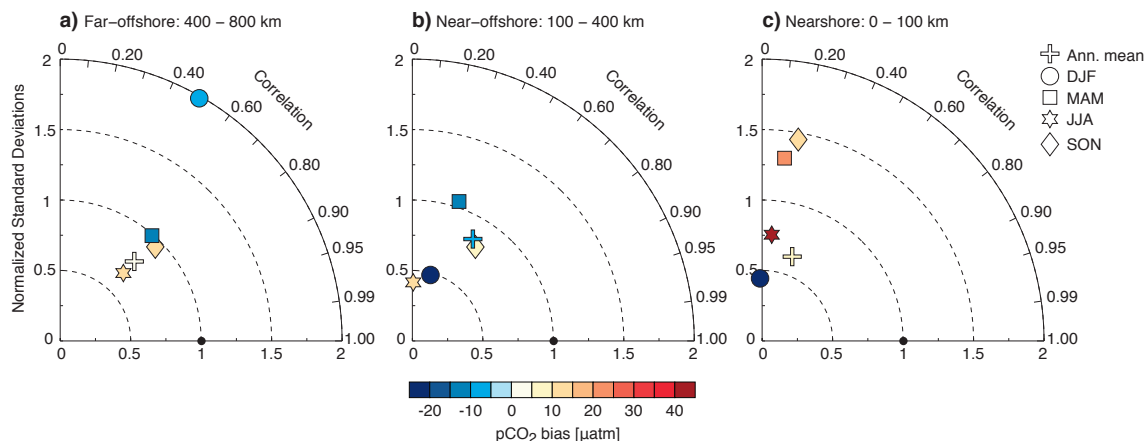


Fig. 3. Taylor diagrams (Taylor, 2001) of modeled vs. observed $p\text{CO}_2$ for the far-offshore (a), near-offshore (b) and nearshore (c) subdomains. Observations are from the Surface Ocean CO_2 Atlas (SOCAT Version 2; Pfeil et al., 2013), the global surface $p\text{CO}_2$ database (Takahashi et al., 2013) and the MBARI/CalCOFI Line 67 (Collins et al., 2003). The distance to the origin point (dashed lines) indicates the modeled field's normalized standard deviation (i.e. a value of 1 would mean a perfect agreement with the observed spatial variability). The angle between each model point and the vertical axis represents the spatial correlation coefficient ("Pearson correlation") for the model vs. the observations. The distance from the observation reference point (black dot) to the model point is that model field's central pattern root-mean square. The color code indicates the bias of the modeled vs. the observed $p\text{CO}_2$: positive values mean the model overestimates $p\text{CO}_2$ and vice versa.

to simulate the observed $p\text{CO}_2$ considerably better than any typical global-scale ocean biogeochemistry model, which often have domain-wide biases of several tens of μatm (e.g., Wanninkhof et al., 2013). However, the model consistently overestimates $p\text{CO}_2$ in the nearshore 100 km, which we verified with various independent databases. We believe this overestimation to be mainly due to deficiencies in our forcing: first, due to the relatively coarse resolution of our wind forcing ($0.25^\circ \times 0.25^\circ$), the wind speed may be overestimated in the nearshore areas (Capet et al., 2004), which would favor more intense coastal upwelling and elevate nearshore $p\text{CO}_2$ levels. Second, our use of climatological forcing results in a nearly continuous upwelling along the coast, while, in reality, periods of intense upwelling are followed by relaxation periods, when ocean biology can reduce surface ocean $p\text{CO}_2$. Errors in our lateral boundary conditions, the model's too low levels of NPP and biases in the nutrient distributions may also help explain the nearshore $p\text{CO}_2$ biases.

4 Sources and sinks for atmospheric CO_2

We model the whole CalCS as a nearly balanced system with regard to atmospheric CO_2 , annually taking up only about $-0.9 \text{ Tg C yr}^{-1}$ over the analysis domain (0–800 km and $\sim 33\text{--}46^\circ \text{ N}$). This corresponds to an average uptake flux density of $-0.05 \text{ mol C m}^{-2} \text{ yr}^{-1}$ (Table 3). This near zero flux hides the presence of strong regional sources and sinks (Figs. 1b, 5): the whole northern subdomain acts as a net sink of $-0.46 \text{ mol C m}^{-2} \text{ yr}^{-1}$ (Fig. 5a), while the cen-

tral and southern subdomains are on average sources with flux densities of 0.04 and $0.16 \text{ mol C m}^{-2} \text{ yr}^{-1}$, respectively (Fig. 5b, c). In the offshore direction, the nearshore 100 km is the strongest source, losing CO_2 to the atmosphere with a flux density of $0.78 \text{ mol C m}^{-2} \text{ yr}^{-1}$ (Table 3). In contrast, the area between 100 and 400 km is the most important contributor to the overall sink with a flux density of $-0.47 \text{ mol C m}^{-2} \text{ yr}^{-1}$. Further offshore of 400 km, the surface ocean is nearly neutral in the annual mean, outgassing on average only $0.05 \text{ mol C m}^{-2} \text{ yr}^{-1}$. Of the individual subdomains, the central nearshore CalCS between Pt. Conception, California, and Cape Blanco, Oregon, is the strongest CO_2 source, with an average flux density of $1.11 \text{ mol C m}^{-2} \text{ yr}^{-1}$, whereas the central area between 100 and 400 km is one of the strongest sink areas with $-0.53 \text{ mol C m}^{-2} \text{ yr}^{-1}$.

In terms of seasonal variability, the strongest outgassing occurs in summer (during the upwelling season) in the nearshore central CalCS (Fig. 5b), while further offshore in summer outgassing is substantially reduced and there is even an uptake in fall. This pattern is also simulated in the northern area, but to a lesser degree (Fig. 5a). Nearly the whole analysis domain acts as a sink for CO_2 in winter and spring, except for the central and southern nearshore domains, which are sources from spring until fall (Fig. 5b, c).

We have not undertaken a systematic investigation of the uncertainties associated with our modeled $p\text{CO}_2$ and air-sea CO_2 fluxes. We did however run additional sensitivity simulations, where we varied either the boundary conditions or some of the model's parameters within their uncertainty to get an indication of the order of magnitude of

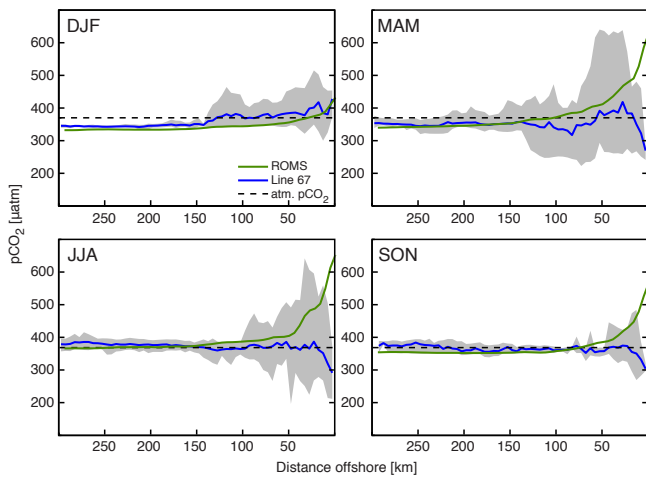


Fig. 4. Seasonally averaged $p\text{CO}_2$ from our model (green line) and from MBARI/CalCOFI Line 67 (blue line) as a function of distance offshore. The gray shaded area represents the range of observed $p\text{CO}_2$ within each season. The dashed black line indicates our model's annual mean atmospheric $p\text{CO}_2$ of $370 \mu\text{atm}$.

this error. Altering the model's DIC boundary conditions by $\pm 10 \text{ mmol C m}^{-3}$, which corresponds to the model's bias in surface DIC that we established in Sect. 3 by comparing to data from the Feely et al. (2008) cruise, resulted in a domain-wide $p\text{CO}_2$ change of approximately $\pm 5 \mu\text{atm}$, with a corresponding air–sea CO_2 flux change of about $\pm 0.2 \text{ mol C m}^{-2} \text{ yr}^{-1}$. Changing the CaCO_3 production ratio from 0.07 to 0.03 and the use of the set of biological parameters of Gruber et al. (2011) instead of those of Gruber et al. (2006) resulted in domain-wide flux changes within the same uncertainty range. Thus, we estimate that the uncertainty associated with our modeled annual mean flux for the whole domain is at least $\pm 0.20 \text{ mol C m}^{-2} \text{ yr}^{-1}$, corresponding to an integrated flux uncertainty of $\pm 3.6 \text{ Tg C yr}^{-1}$ (Table 3). This estimate does not include the effect of potential $p\text{CO}_2$ biases of our model, particularly those in the nearshore regions. The nearshore bias of around $10 \mu\text{atm}$ causes roughly an error in the CO_2 flux of $0.4 \text{ mol C m}^{-2} \text{ yr}^{-1}$. Thus, if we were to subtract this bias uniformly from our model simulated $p\text{CO}_2$, our net outgassing in the nearshore 100 km would be nearly halved to around $0.4 \text{ mol C m}^{-2} \text{ yr}^{-1}$. However, we do not apply such a correction given the substantial uncertainty associated with the determination of the model bias.

Our uncertainty estimate also does not include the potential impact of variable stoichiometric C : N ratios for phytoplankton growth. Martiny et al. (2013) showed that these ratios may vary systematically, with oligotrophic gyres having larger than Redfield ratios and nutrient-replete systems having lower than Redfield ratios. While we do not expect a substantial effect of such systematic variations in the C : N ratios on the overall budget of the CalCS, they will nevertheless quite certainly affect the local fluxes. We would expect

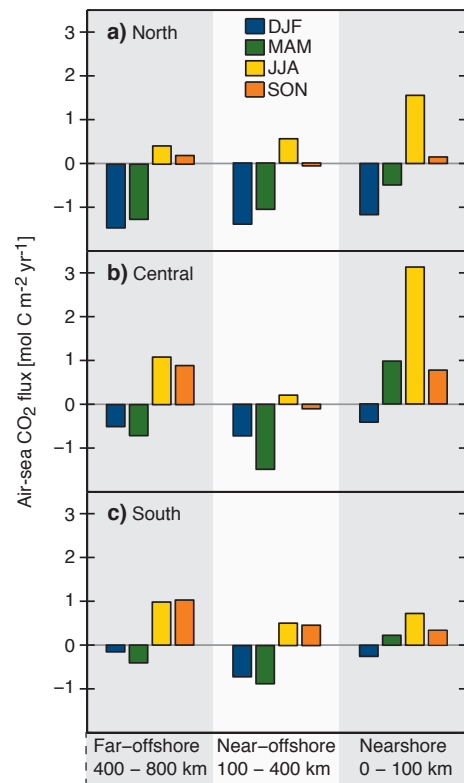


Fig. 5. Seasonally averaged air–sea CO_2 flux for the northern (a), central (b) and southern (c) subdomains in the nearshore, near-offshore and far-offshore regions. Positive values denote an outgassing of CO_2 , negative values an uptake by the surface ocean.

a larger outgassing in the nearshore regions, as the tendency for lower than Redfield C : N ratio in such nutrient replete systems would cause a lower carbon drawdown, permitting a larger fraction of the upwelled carbon to escape to the atmosphere. In contrast, in the oligotrophic offshore regions, we would expect a stronger uptake of CO_2 from the atmosphere, as the higher than Redfield C : N ratio would tend to lead to lower $p\text{CO}_2$. Overall, we would expect a stronger onshore–offshore gradient, but not a large change in the net flux over the entire study region. A more quantitative assessment of the effect of using a variable C : N ratio would require a more detailed, separate analysis with additional sensitivity simulations.

Our domain's mean flux density of $-0.05 \pm 0.20 \text{ mol C m}^{-2} \text{ yr}^{-1}$ agrees best with the results of Chavez et al. (2007), who suggested the whole west coast of the US to act as a nearly balanced, small source of $0.03 \text{ mol C m}^{-2} \text{ yr}^{-1}$. However, the flux densities of the individual subdomains agree more with the findings of Evans et al. (2011), who showed that the Oregon coast (which is to the largest part included in our northern subdomain) acts as an annual net sink of $-0.3 \text{ mol C m}^{-2} \text{ yr}^{-1}$, and with the results of Pennington et al. (2010), who found that the central California region is nearly balanced. All of the

subdomains experience a sign change in CO_2 fluxes during the course of a year, which is consistent with the findings of Hales et al. (2012).

In order to compare our air–sea CO_2 fluxes more directly to Hales et al. (2012), we average our results over only the first 0–400 km. This yields an average uptake flux density of $-0.17 \text{ mol C m}^{-2} \text{ yr}^{-1}$, which is smaller than their result of $-0.66 \text{ mol C m}^{-2} \text{ yr}^{-1}$ over a similar region. However, given the sizable errors in the estimate by Hales et al. (2012) as well as ours, the two estimates are actually statistically indistinguishable. They both agree that the CalCS is essentially neutral with regard to atmospheric CO_2 or a small sink at best.

These comparisons demonstrate that while the net CO_2 flux over the entire CalCS is relatively small, the fluxes vary strongly in space and time, in accordance with findings from several of the previous studies (e.g., Hales et al., 2005; Chavez et al., 2007; Evans et al., 2011; Hales et al., 2012).

The air–sea CO_2 flux pattern is almost entirely driven by surface ocean $p\text{CO}_2$, which exhibits strong regional differences (Fig. 1a, Table 3). Compared to surface ocean $p\text{CO}_2$, variations in atmospheric $p\text{CO}_2$ are very small (e.g., Komhyr et al., 1985; Conway et al., 1994) and variations in the gas transfer velocity and in the CO_2 solubility are of secondary importance, as they only tend to modulate the magnitude of air–sea CO_2 fluxes without influencing their sign (Eq. 1).

5 Spatial variability of annual mean $p\text{CO}_2$

To highlight the spatial variability of the annual mean surface ocean $p\text{CO}_2$, we subtract its domain average and consider spatial anomalies only (Fig. 6a). Two distinct features can be identified in Fig. 6a, which is very close to the pattern of the air–sea $p\text{CO}_2$ difference (not shown), given that the domain average $p\text{CO}_2$ differs little from atmospheric $p\text{CO}_2$: (i) large positive anomalies are found in the upwelling area along the coast of the central CalCS, and (ii) there is a division around 38° N between the northern part of the model domain, which tends to have negative anomalies, and the southern part with positive anomalies.

The analysis of the drivers behind this pattern reveals that this pattern is largely a result of strong spatial gradients in DIC^s and T (Fig. 6b, d), with Alk^s having a smaller role and FW fluxes being unimportant (Fig. 6c, e). The strong north–south gradients induced by DIC^s and T tend to cancel each other substantially, so that the largely unopposed onshore–offshore gradient of DIC^s becomes a prominent feature in the annual mean distribution of $p\text{CO}_2$. An exception to this general pattern is the Southern California Bight, where the contribution of Alk^s is important, tending to oppose the effect of DIC^s .

The identification of the processes underlying the spatial pattern in $p\text{CO}_2$ permits us to better understand what drives these gradients, in particular those of the key driver DIC^s

(Fig. 7). This process-based separation based on the sensitivity studies (Table 2) reveals that the most important contributions to the spatial gradients of annual mean $p\text{CO}_2$ are circulation and biological production (Fig. 7a, b), both of which act upon DIC and Alk. Circulation, i.e. the transport of high DIC and Alk from the boundaries into the domain's interior and then to the surface, leads to high surface ocean $p\text{CO}_2$ values far exceeding atmospheric $p\text{CO}_2$ over most of the domain (Fig. 7a). The high DIC in the upwelled waters pushes surface $p\text{CO}_2$ up to values around $700 \mu\text{atm}$ in the upwelling area and between 400 and $600 \mu\text{atm}$ further offshore. In the central domain, high $p\text{CO}_2$ values extend particularly far offshore: values of $550 \mu\text{atm}$ can still be found around 400–500 km offshore. This large offshore extent is caused by the intense offshore Ekman and eddy-driven transport in the central CalCS (Nagai et al.), which is not strongly opposed by the biological removal of DIC. The upwelled waters are also enriched in Alk, which acts to reduce the impact of the upwelling of DIC on surface ocean $p\text{CO}_2$, but this effect is substantially smaller (not shown).

The biological fixation of CO_2 and the subsequent transport of the fixed carbon to depth opposes the circulation effect and acts to decrease $p\text{CO}_2$ nearly everywhere by around $160 \mu\text{atm}$ on average (Fig. 7b). This biologically induced $p\text{CO}_2$ drawdown is generally largest in the nearshore region. Yet, unlike physical circulation, whose effects are largest in the upwelling area of the central CalCS and decrease with increasing distance to the coast, the biologically driven $p\text{CO}_2$ drawdown is highest between 50 and 100 km offshore in the central CalCS and extends farther offshore than the physical circulation-driven maximum. This results in the biological compensation of circulation effects being much weaker in the first 50 km nearshore region of the central CalCS in comparison to the rest of the domain. The spatial decoupling between the area of maximum upwelling and the region of maximum biological production has been documented in previous studies of the CalCS and was linked to the large upwelling-driven offshore fluxes of nutrients, which are not fully utilized in the coastal upwelling zone (Gruber et al., 2011; Lachkar and Gruber, 2011). The combined effect of circulation and biological production, which we will refer to here as the “biological loop”, is hence largest in the first 50–100 km, with values of $500\text{--}650 \mu\text{atm}$ (Fig. 7c). Offshore of 100 km, the contribution of the biological loop is nearly homogeneous at around $350 \mu\text{atm}$, i.e. below atmospheric CO_2 .

In contrast to circulation and biology, the contribution by the air–sea CO_2 flux is comparatively small, contributing $\pm 30 \mu\text{atm}$ (Fig. 7d). This pattern is directly tied to the regions where the CalCS acts as a source or sink for atmospheric CO_2 (see Fig. 1b). The contribution by the processes affecting the solubility of CO_2 is somewhat larger, amounting to spatial gradients in $p\text{CO}_2$ of up to $\pm 50 \mu\text{atm}$ (Fig. 7e). This contribution very closely resembles that associated with the T driver (compare with Fig. 6d). This is

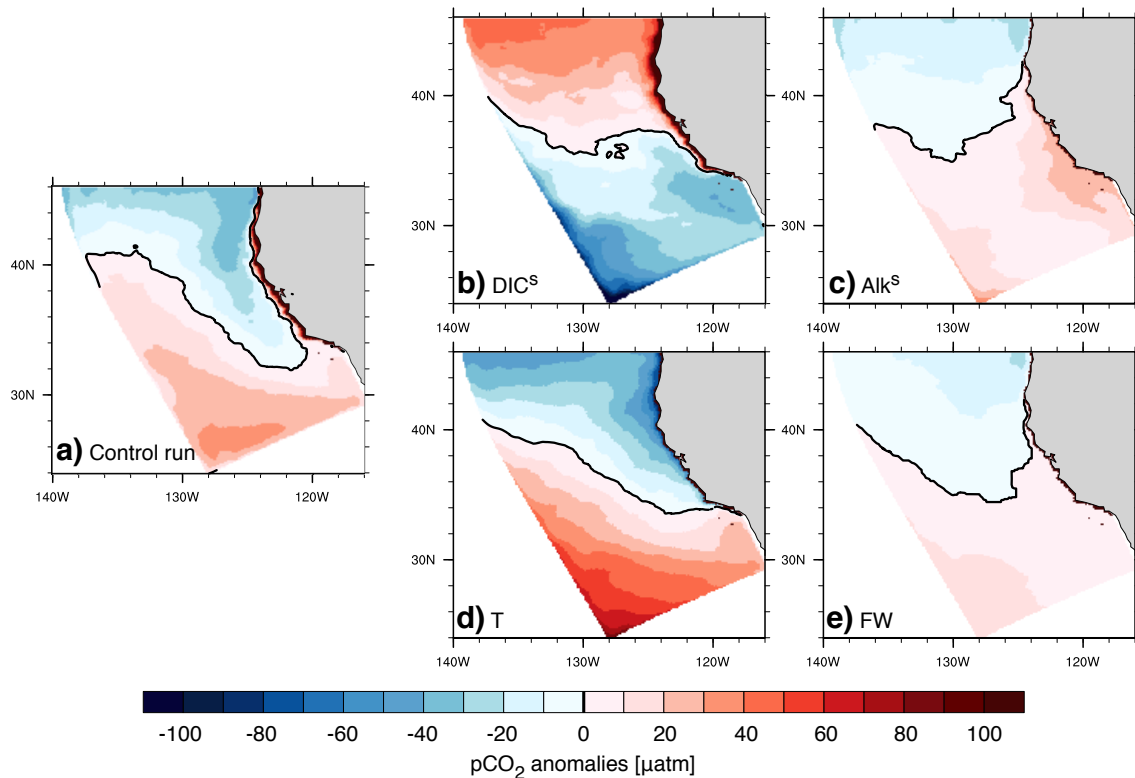


Fig. 6. Spatial $p\text{CO}_2$ anomalies computed as the difference between in situ and domain mean $p\text{CO}_2$. Panel (a) shows total $p\text{CO}_2$ anomalies in the control simulation and panels (b–e) show the contributions of the four drivers DIC^{S} , Alk^{S} , T and FW to the total.

because variations in T dominate the variations in the CO_2 solubility, while the contribution of FW is very small.

In summary, the net effect of circulation and biological productivity, i.e. the contribution of the biological loop, controls to a large extent the distribution of $p\text{CO}_2$, with small differences in the spatial pattern between these two opposing tendencies explaining much of the onshore–offshore gradient. This is because these small differences explain the spatial distribution of DIC^{S} , the most important driver for the spatial distribution of $p\text{CO}_2$. This also explains the very high $p\text{CO}_2$ values found in the 50 km wide coastal strip in the central CalCS as well as the rapid decrease of $p\text{CO}_2$ with increasing distance to the coast in that region (see Fig. 1a). The processes affecting solubility, i.e. primarily surface ocean T , explain most of the north–south gradient in surface ocean $p\text{CO}_2$, since the combined effect of circulation and biology shows nearly no spatial gradient in the offshore regions, and the air–sea CO_2 flux is largely unimportant.

As $p\text{CO}_2$ and the air–sea CO_2 fluxes vary not only on a spatial scale but show also high temporal variability, we next investigate the drivers and processes behind the seasonal and nonseasonal components of $p\text{CO}_2$ variability.

6 Temporal $p\text{CO}_2$ variability

6.1 Seasonal variability

Surface ocean $p\text{CO}_2$ in the CalCS varies substantially in time with a standard deviation of up to $\pm 100 \mu\text{atm}$ in the nearshore 0–100 km (Fig. 8a). The standard deviation tapers off quite quickly with increasing offshore distance with typical values of about 10–40 μatm in the regions further offshore. A good part of this variability is driven by the seasonal cycle (Fig. 8b), especially in the offshore region, where it accounts for almost all of the variability.

To investigate the seasonality of surface ocean $p\text{CO}_2$, we subtract the annual mean $p\text{CO}_2$ from the simulated monthly climatology and consider $p\text{CO}_2$ seasonal anomalies and their drivers following the same approach used for studying the spatial pattern. To capture the contrasting features of $p\text{CO}_2$ seasonality between the coastal and open ocean regions, we analyze nearshore-averaged (less than 100 km offshore) and offshore-averaged temporal anomalies separately. In both the nearshore and offshore regions, positive anomalies of $p\text{CO}_2$ prevail during summer and early fall whereas negative anomalies are observed during the winter and in early spring (black lines in Figs. 9 and 10).

The decomposition of the $p\text{CO}_2$ seasonal anomalies into individual contributions associated with changes in DIC^{S} ,

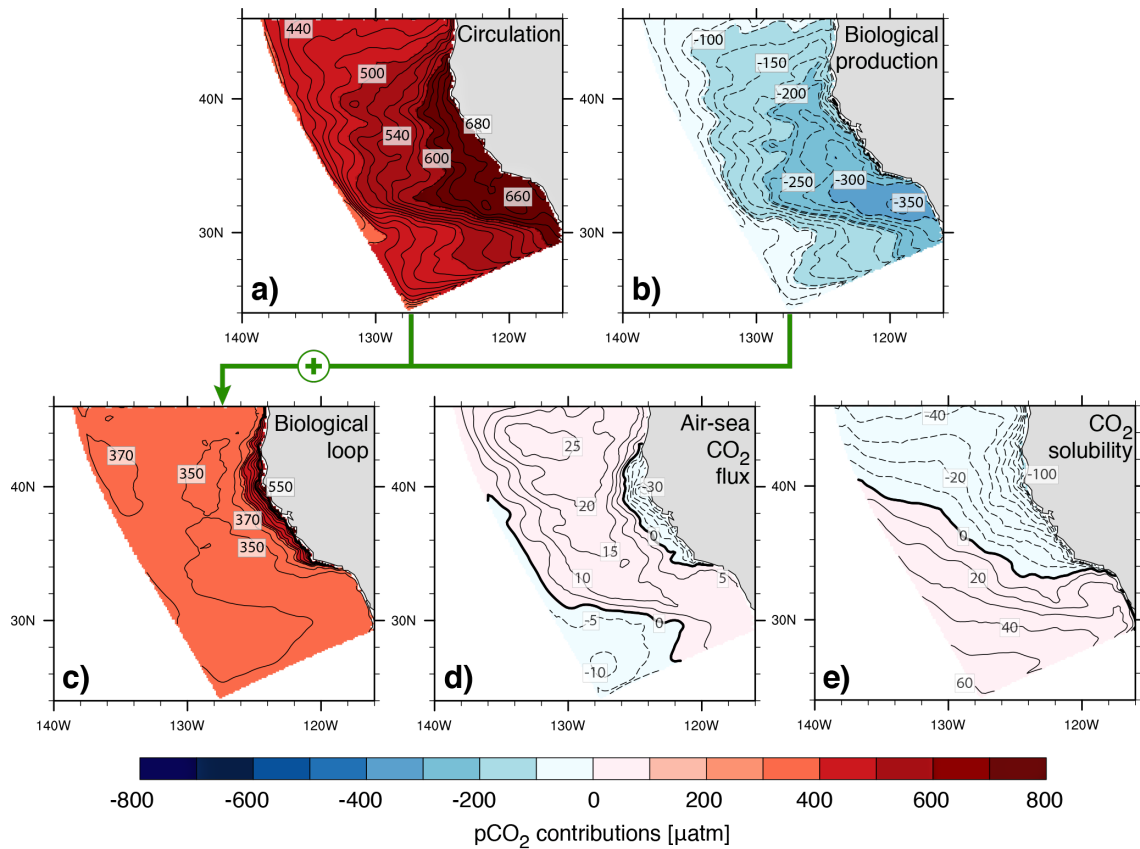


Fig. 7. Contributions of ocean circulation (a), biological production (b), air-sea CO_2 flux (d) and CO_2 solubility (e) to annual mean $p\text{CO}_2$ as simulated in the control simulation. Panel (c) represents the contribution of the biological loop, i.e. the sum of (a) and (b) (indicated by the green line). Positive contributions are displayed as solid lines, negative contributions as dashed lines.

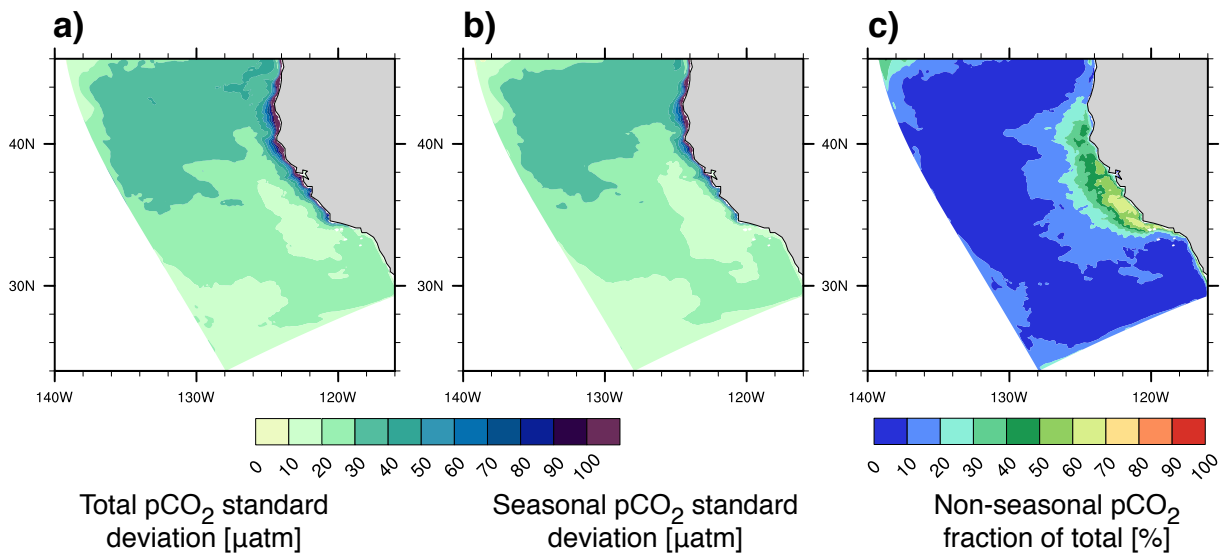


Fig. 8. Total $p\text{CO}_2$ standard deviation (a) computed from 2-day output spanning seven consecutive model years, and seasonal $p\text{CO}_2$ standard deviation (b) derived from a fitted mean over the same seven years. Panel (c) shows the fraction of the total $p\text{CO}_2$ variance (square of the standard deviation) attributable to nonseasonal variability, i.e. the difference between total and seasonal $p\text{CO}_2$ variance divided by the total variance (shown in percent).

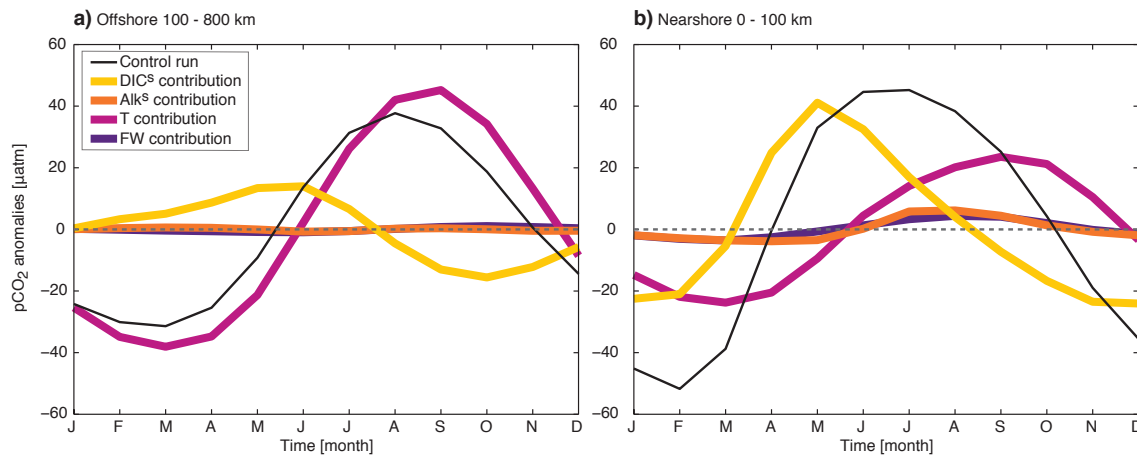


Fig. 9. Monthly mean $p\text{CO}_2$ anomalies for the offshore (a) and the nearshore (b) domains: the colored lines represent the contributions of the four drivers DIC^{S} , Alk^{S} , T and FW to monthly mean $p\text{CO}_2$ anomalies from the control simulation (black line).

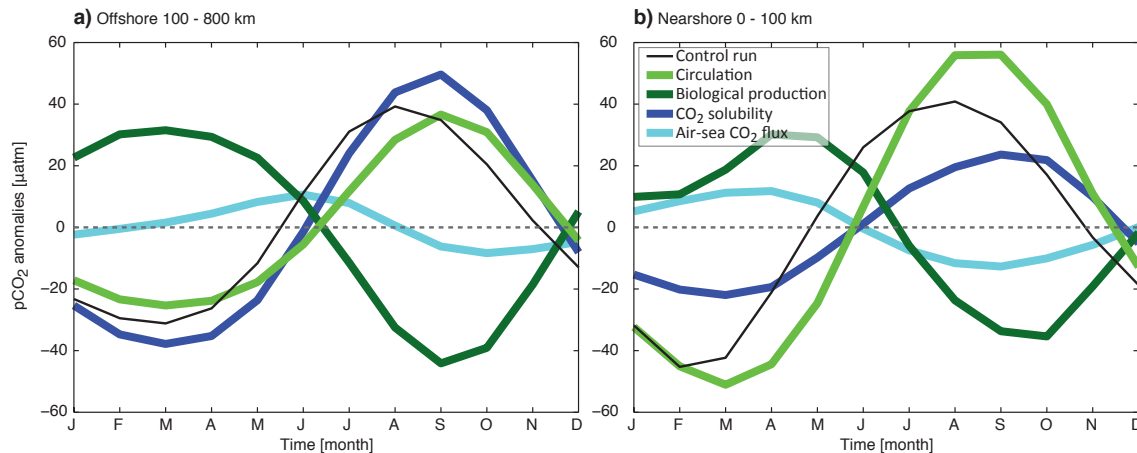


Fig. 10. Monthly mean $p\text{CO}_2$ anomalies for the offshore (a) and the nearshore (b) domains: the colored lines represent the contributions of ocean circulation, biological production, CO_2 solubility and air-sea CO_2 flux to monthly mean $p\text{CO}_2$ anomalies from the control simulation (black line).

Alk^{S} , T and FW (Fig. 9) shows that the seasonal variability of $p\text{CO}_2$ in the two regions is driven by distinctly different combinations, whose relative contributions to the seasonal cycle are similar to the contributions discussed for the spatial pattern. In the offshore region, the seasonal cycle is to a very large extent caused by the seasonality of T , i.e. by the seasonal cycle of warming and cooling (Fig. 9a). The $p\text{CO}_2$ variations driven by DIC^{S} tend to have an opposing seasonal cycle, thereby flattening the simulated $p\text{CO}_2$ relative to that purely driven by T . In contrast, the $p\text{CO}_2$ seasonality in the nearshore region is caused by variations in both T and DIC^{S} – and to a lesser degree variations in Alk^{S} and in the FW fluxes (Fig. 9b). Here, the DIC^{S} -driven variations are about four months out of phase with those of T , causing primarily a phase shift of the $p\text{CO}_2$ seasonality relative to the purely T -driven seasonal cycle. The seasonal cycle of the

Alk^{S} -driven component is characterized by higher modes, i.e. further modifying the modeled seasonal cycle of $p\text{CO}_2$.

As was the case for the spatial distribution of $p\text{CO}_2$, we can gain further insight into the working of the seasonal cycle of $p\text{CO}_2$ by analyzing the processes behind it, i.e. by determining the contributions of the air-sea CO_2 flux, ocean biology, CO_2 solubility, and ocean circulation.

In the offshore domain, the processes controlling CO_2 solubility contribute most to the seasonal $p\text{CO}_2$ variability (Fig. 10a). In this region, the contributions of circulation and biology tend to nearly perfectly balance each other, whereas the air-sea CO_2 flux acts to slightly reduce the overall amplitude of the $p\text{CO}_2$ seasonal cycle. In contrast, in the nearshore region, circulation, i.e. essentially upwelling, is the most important driver of $p\text{CO}_2$ seasonality (Fig. 10b). Biological production tends to counteract the circulation effect particularly in spring and early summer. Yet, this biological

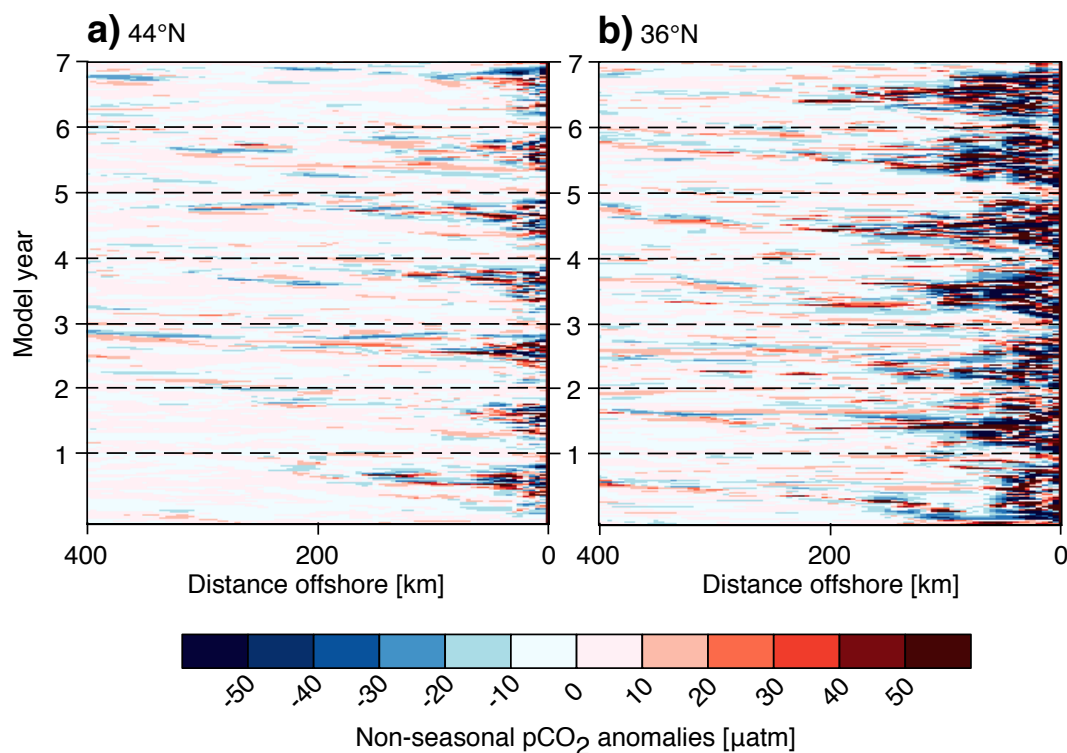


Fig. 11. Hovmöller diagrams representing nonseasonal $p\text{CO}_2$ anomalies as a function of distance offshore, based on 2-day output spanning seven consecutive model years. The anomalies were computed as the difference between the total $p\text{CO}_2$ over the seven analysis years and a seasonal fitted mean over the same seven years. Panel (a) shows a transect at around 44°N , while panel (b) depicts a transect at around 36°N . The transects run roughly along the midlines of the northern and central subdomains, respectively.

compensation is only partial, especially during winter when biology has little effect on $p\text{CO}_2$. The seasonal variations in CO_2 solubility also play an important role in the nearshore region, but are less prominent than in the offshore region. Finally, similarly to its role in the offshore region, the air–sea CO_2 flux acts throughout the year to dampen the seasonal cycle of $p\text{CO}_2$.

In conclusion, the simulated seasonality of $p\text{CO}_2$ emerges from the degree of compensation between the solubility-driven $p\text{CO}_2$ variations associated with the seasonal cooling and heating of the surface waters as well as the combined circulation- and biology-driven variations affecting surface ocean DIC^s and hence $p\text{CO}_2$. In the offshore region, the solubility-driven variations clearly dominate, while circulation/biology can only dampen the seasonality somewhat. In the nearshore regions, the circulation/biology-driven variations are of nearly the same amplitude, but out of phase, leading to a complex seasonal cycle in $p\text{CO}_2$.

6.2 Mesoscale variability

Figure 8 highlights that although the seasonal component accounts for most of the total $p\text{CO}_2$ variability in the offshore regions, a substantial fraction of the total variability in the nearshore regions is driven by the nonseasonal compo-

nent (Fig. 8c, shown in percent). Our model results demonstrate that the nonseasonal component is the dominant variability mode in the first 100–200 km offshore of the central CalCS, explaining up to 70 % of the total $p\text{CO}_2$ variability (Fig. 8c). Most of this variability is driven by mesoscale activity, which is more intense in the upwelling regions due to stronger baroclinic instabilities. To further investigate the eddy-driven component of our modeled $p\text{CO}_2$ variability, we analyze the nonseasonal $p\text{CO}_2$ component as a function of time and offshore distance (Fig. 11): a comparison of the northern and central offshore transects confirms that the activity attributable to mesoscale and nonseasonal processes is much more prominent in the central area (Fig. 11b), which displays year-round strong eddy activity often reaching out up to 200 km offshore, whereas in the north (Fig. 11a) the eddy activity is detectable only on a seasonal timescale, starting in late summer or early fall. In general, for both domains, strong offshore transport occurs most frequently around the middle of the year. We do not show any transects for the southern subdomain, as any activity attributable to mesoscale eddies was negligible there compared to the other two subdomains.

This high variability associated with eddy activity, which is especially pronounced in the nearshore area, leads to

relatively short temporal and spatial decorrelation scales, requiring relatively dense sampling in time and space in order to fully capture the true $p\text{CO}_2$ signal. In the open ocean, Jones et al. (2012) showed that $p\text{CO}_2$ can be correlated over distances of several hundred kilometers, but pointed out that these scales are much shorter in the coastal ocean, perhaps as short as a few tens of kilometers in space and from a few days to weeks in time.

Without a full Observing System Simulation Experiment, we are not in the position to make accurate recommendations with regard to how the current network would have to be expanded to capture the mean flux and its variability with good confidence. Nevertheless, we can make some qualitative, general statements, based on our model-based experience. First, the presently available observations are likely sufficient to estimate the domain-wide climatological annual mean air–sea CO_2 flux, as indicated by the relatively good agreement between the most recent estimates. Second, the current network is with good confidence insufficient to determine variability in time and space around this mean flux. In order to achieve this, the network would mainly need to be expanded in the first 100 km, where the short temporal and spatial decorrelation length scales require a denser coverage of $p\text{CO}_2$ and air–sea CO_2 flux measurements. It would furthermore be highly desirable to have a more complete latitudinal coverage of the nearshore area of the entire west coast of the US, whose current observational coverage is at best fragmentary. To this end, alongshore underway cruises, rather than moored stations, may provide the most adequate means of measuring $p\text{CO}_2$ within this extended area of interest.

Given that our model is forced with monthly climatologies at the surface and at the lateral boundaries, the fraction of nonseasonal variability is likely underestimated in our simulations. This is because neither long-term variability such as interannual or -decadal variability nor very high frequency variability associated with weather systems are included in our forcing. Sub-mesoscale processes like filaments and fronts, which cannot be properly resolved at our model resolution, may further lead to an underestimation of the level of nonseasonal $p\text{CO}_2$ variability in our model. We thus refer to a future study for a more detailed assessment of the required sampling density in order to fully capture the true variability of $p\text{CO}_2$ and the associated air–sea CO_2 fluxes.

7 Discussion

Several questions emerge from our finding that the strong sources and sinks within the CalCS sum up to a nearly balanced system overall with regard to atmospheric CO_2 . First, does this near complete spatial compensation occur by chance, or are there some underlying mechanisms at play? Second, if such underlying mechanisms exist, how might

they control the air–sea CO_2 balance under future climate change? Third, what is the contribution of the oceanic uptake of anthropogenic CO_2 to the overall source/sink balance? Fourth, how do the air–sea CO_2 fluxes within the CalCS compare to fluxes elsewhere, and in particular, how do these results fit into the global picture?

Our analysis of the mechanisms underlying the annual mean air–sea CO_2 fluxes reveals that the near complete spatial compensation is a result of ocean productivity very closely compensating the effect of ocean circulation on the air–sea CO_2 flux. This compensation is not fortuitous, as these two processes are fundamentally linked to each other. This is because they represent the two components of the biological loop, i.e. the downward component, which is usually referred to as the biological pump (Volk and Hoffert, 1985) and is largely caused by the downward export of organic matter, and the upward component driven by the upward mixing and transport of the DIC- and Alk-rich deeper waters to the surface (Gruber and Sarmiento, 2002; Sarmiento and Gruber, 2006). As the upward component tends to control also the supply of the limiting nutrient to the near surface ocean, and hence also determines to a large degree the magnitude of biological productivity, the upward and downward components of the biological loop are strongly coupled with each other. The efficiency of the biological pump, i.e. the efficiency with which the upward supplied limiting nutrient is biologically taken up and exported downward again, is a good indicator of the strength of this linkage (Sarmiento and Gruber, 2006). In the CalCS, where nitrate tends to be the limiting nutrient (Eppley and Peterson, 1979), the nitrate use efficiency turns out to be very high, as evidenced by the near complete consumption of nitrate in the offshore region. This implies also a very high efficiency of the biological pump, and hence a tendency for an overall near complete compensation between the effects of biology and circulation. This does not occur regionally: in the very nearshore, the nutrient use efficiency is relatively low, allowing a part of the upwelled DIC to escape into the atmosphere. However, as these waters “age” while they are being transported further offshore, the biological pump operates so efficiently that all nitrate is fully utilized, creating the conditions for some of the escaped CO_2 to be taken up again by the surface ocean (e.g., Hales et al., 2005; Feely et al., 2008; Pennington et al., 2010; Fassbender et al., 2011).

These arguments depend, of course, critically on the near constancy of the stoichiometric C : N ratio of phytoplankton growth. Any carbon over- or underconsumption relative to our assumed Redfield ratio of 106 : 16 would permit the biologically driven component of the air–sea CO_2 fluxes to decouple from the efficiency of the biological pump. But as we argued above, we expect the potentially systematic tendencies of this ratio to have a relatively small effect on the whole domain air–sea CO_2 fluxes. While the nearshore carbon underconsumption makes the biological pump less efficient there, the tendency for carbon overconsumption in the offshore, which enhances the efficiency, may largely

compensate for it, resulting in little overall change. This is rather speculative, and a more thorough assessment of the effect of systematic variations in the stoichiometric ratios on the air–sea CO_2 fluxes is clearly needed. But our current understanding of the underlying processes controlling these ratios is poor, preventing us from following this path.

Regardless of the uncertainty arising from the stoichiometric ratios, the efficiency of the biological pump might change in the future under climate change-driven perturbations such as upwelling-favorable wind intensification and increased stratification. For example, Lachkar and Gruber (2013) show that increasing upwelling-favorable winds results in a decrease in the biological pump efficiency, and hence an increase in the CO_2 outgassing. This is because the large increase in outgassing associated with the upwelling intensification outweighs the effects of the concurrent increase in productivity on surface $p\text{CO}_2$.

It is important to recognize that the anthropogenic perturbation of atmospheric CO_2 has perturbed the air–sea CO_2 fluxes in the CalCS. By comparing our simulations to one where we had set atmospheric CO_2 to a preindustrial value of $280 \mu\text{atm}$ (Gruber et al., 2012; Hauri et al., 2013), we estimate the domain mean uptake flux of anthropogenic CO_2 in the CalCS to be about $-1 \text{ mol C m}^{-2} \text{ yr}^{-1}$, which is about twice as large as the global mean (e.g., Mikaloff Fletcher et al., 2006; Gruber et al., 2009; Wanninkhof et al., 2013). This is not unexpected given that upwelling regions tend to be places of stronger than normal uptake of anthropogenic CO_2 from the atmosphere, largely as a consequence of them transporting waters to the surface that have not seen the atmosphere for some time. This substantial uptake flux of anthropogenic CO_2 implies that the entire CalCS in preindustrial times was a small to moderate net source of CO_2 to the atmosphere.

The different processes controlling surface ocean $p\text{CO}_2$ operate in the CalCS in a manner that is similar to how they impact surface ocean $p\text{CO}_2$ on the global scale, as also there the interaction of ocean circulation and biology is a primary determinant of the spatial distribution of the air–sea CO_2 fluxes (e.g., Gruber and Sarmiento, 2002; Toggweiler et al., 2003; Sarmiento and Gruber, 2006; Gruber et al., 2009). Globally, circulation in the absence of biology tends to increase $p\text{CO}_2$ everywhere, with the efficiency of the biological pump ultimately determining how strong the opposing effect of biology ends up being, i.e. whether a particular region becomes a source or a sink of CO_2 , with regard to the biological loop. In the CalCS, the high degree of nutrient utilization and the implied high efficiency of the biological pump suggests that this region operates more like the temperate to sub-polar North Atlantic, where the biologically induced fluxes are overall small, and very unlike the North Pacific, where a low nutrient utilization leads to a substantial net outgassing of CO_2 associated with the biological loop (Gruber et al., 2009). We expect also the Canary Current System to operate very similarly to the CalCS given the observed complete nu-

trient utilization there. In contrast, we expect the Humboldt Current System, where nitrate is often not very efficiently used due to iron limitation, to have a strong net outgassing caused by the inefficient biological pump.

8 Summary and outlook

We used a series of eddy-resolving simulations of the CalCS (i) to assess the climatological mean air–sea CO_2 fluxes and their spatiotemporal variability and (ii) to determine the drivers and processes behind the variability of these fluxes and ultimately surface ocean $p\text{CO}_2$.

Our model results demonstrate that the CalCS is essentially balanced in terms of air–sea CO_2 fluxes, with a very small net uptake flux density of $-0.05 \pm 0.20 \text{ mol C m}^{-2} \text{ yr}^{-1}$. The fluxes vary strongly locally and on a seasonal timescale, with the nearshore 100 km losing a substantial amount of CO_2 to the atmosphere, which is largely compensated by biologically driven uptake in the regions offshore of 100 km. We interpret this strong spatial compensation to be the result of a highly efficient biological pump, as indicated by the complete utilization of the upwelled limiting nutrient, nitrate. The CalCS acts also as a substantial sink for anthropogenic CO_2 , taking up approximately $-1 \text{ mol C m}^{-2} \text{ yr}^{-1}$, implying that the CalCS was a weak source of CO_2 to the atmosphere in preindustrial times.

Nearly all of the variability in air–sea CO_2 fluxes is caused by surface ocean $p\text{CO}_2$, whose seasonal variability dominates over most of the offshore areas, while in the nearshore 100 km most of the variability is determined by subseasonal, mesoscale activity. The variability in the nearshore is mostly associated with circulation and biological production, which affect DIC, Alk and T , while air–sea CO_2 fluxes, CO_2 solubility and FW fluxes play a minor role. However, offshore of 100 km, changes in T are the most important drivers of $p\text{CO}_2$ variability.

One of the main caveats of our model study is that we neither include high frequency forcing associated with weather-related events, nor longer-term interannual variability. We aim to address this issue in a future study by adding such forcing to our model. We also plan to include an analysis of spatial and temporal decorrelation length scales in order to assess the required sampling density for accurately determining the source/sink nature of the CalCS.

Although we made through our model-based study substantial progress in determining the source/sink nature of the CalCS and the mechanisms underlying it, it would be highly desirable to verify this with observations. Clearly, the current network is largely inadequate for this purpose, and would have to be substantially strengthened. Furthermore, accurate quantification of the net air–sea CO_2 fluxes in the CalCS is also becoming increasingly important in the context of CO_2 inversion studies that aim to verify the emissions

of anthropogenic CO_2 in California through measurements of atmospheric CO_2 . This is because the large and highly variable air–sea CO_2 fluxes leave a substantial imprint on atmospheric CO_2 , which has to be well quantified before the emissions can be inferred. Together with the observations, the models need to be further developed and refined, as they permit us to put the observations into a spatiotemporal context, and help assess the relevant processes.

Acknowledgements. This research was financially supported by the Swiss Federal Institute of Technology Zürich (ETH Zürich) and through EU FP7 project CARBOCHANGE – Changes in carbon uptake and emissions by oceans in a changing climate – which received funding from the European Commission’s Seventh Framework Programme under grant agreement no. 264879. All simulations were performed at the central computing cluster of ETH Zürich, Brutus. We are grateful to the ROMS and NPZD developers in general, and thank in particular M. Münnich, D. Loher and L. Kropuenske-Artman from ETH Zürich for their invaluable help and support, and G.-K. Plattner for some of the initial analyses. We also thank B. Hales for kindly providing us with his $p\text{CO}_2$ data, F. P. Chavez for sharing $p\text{CO}_2$ measurements from the MBARI/CalCOFI Line 67, R. A. Feely for granting us access to his cruise database (doi:10.3334/CDIAC/otg.CLIVAR_NACP_West_Coast_Cruise_2007) and the SOCAT and LDEO teams for making their global $f\text{CO}_2$ and $p\text{CO}_2$ data sets available to us. The authors are also grateful to two anonymous referees for their valuable comments and suggestions, which have helped improve the quality and clarity of this manuscript.

Edited by: L. Cotrim da Cunha

References

- Bograd, S. J., Schroeder, I., Sarkar, N., Qiu, X., Sydeman, W. J., and Schwing, F. B.: Phenology of coastal upwelling in the California Current, *Geophys. Res. Lett.*, 36, L01602, doi:10.1029/2008GL035933, 2009.
- Borges, A., Delille, B., and Frankignoulle, M.: Budgeting sinks and sources of CO_2 in the coastal ocean: Diversity of ecosystems counts, *Geophys. Res. Lett.*, 32, L14601, doi:10.1029/2005GL023053, 2005.
- Cai, W.-J., Dai, M., and Wang, Y.: Air-sea exchange of carbon dioxide in ocean margins: A province-based synthesis, *Geophys. Res. Lett.*, 33, L12603, doi:10.1029/2006GL026219, 2006.
- Capet, X. J., Marchesiello, P., and McWilliams, J. C.: Upwelling response to coastal wind profiles, *Geophys. Res. Lett.*, 31, L13311, doi:10.1029/2004GL020123, 2004.
- Chan, F., Barth, J. A., Lubchenco, J., Kirincich, A., Weeks, H., Peterson, W. T., and Menge, B. A.: Emergence of anoxia in the California Current large marine ecosystem, *Science*, 319, 920, doi:10.1126/science.1149016, 2008.
- Chavez, F. P. and Messié, M.: A comparison of Eastern Boundary Upwelling Ecosystems, *Prog. Oceanogr.*, 83, 80–96, 2009.
- Chavez, F. P., Takahashi, T., Cai, W.-J., Friederich, G., Hales, B., Wanninkhof, R., and Feely, R. A.: Coastal Oceans, in: *The First State of the Carbon Cycle Report (SOCCR): The North American Carbon Budget and Implications for the Global Carbon Cycle. A Report by the US Climate Change Science Program and the Subcommittee on Global Change Research*, edited by: King, A., Dilling, L., Zimmerman, G., Fairman, D., Houghton, R., Marland, G., Rose, A., and Wilbanks, T., chap. 15, National Oceanic and Atmospheric Administration, National Climatic Data Center, Asheville, NC, USA, 157–166, 2007.
- Collins, C., Pennington, J., Castro, C., Rago, T., and Chavez, F. P.: The California Current system off Monterey, California: physical and biological coupling, *Deep-Sea Res. Pt. II*, 50, 2389–2404, 2003.
- Conway, T. J., Tans, P. P., Waterman, L. S., Thoning, K. W., Kitzis, D. R., Masarie, K. A., and Zhang, N.: Evidence for interannual variability of the carbon cycle from the National Oceanic and Atmospheric Administration/Climate Monitoring and Diagnostics Laboratory Global Air Sampling Network, *J. Geophys. Res.*, 99, 22831–22855, 1994.
- Dickson, A. G. and Millero, F. J.: A comparison of the equilibrium constants for the dissociation of carbonic acid in seawater media, *Deep-Sea Res. Pt. I*, 34, 1733–1743, 1987.
- Doney, S. C., Lima, I., Feely, R. A., Glover, D. M., Lindsay, K., Mahowald, N., Moore, J. K., and Wanninkhof, R.: Mechanisms governing interannual variability in upper-ocean inorganic carbon system and air–sea CO_2 fluxes: Physical climate and atmospheric dust, *Deep-Sea Res. Pt. II*, 56, 640–655, 2009.
- Eppley, R. W. and Peterson, B. J.: Particulate organic matter flux and planktonic new production in the deep ocean, *Nature*, 282, 677–680, doi:10.1038/282677a0, 1979.
- Evans, W., Hales, B., and Strutton, P. G.: Seasonal cycle of surface ocean $p\text{CO}_2$ on the Oregon shelf, *J. Geophys. Res.*, 116, C05012, doi:10.1029/2010JC006625, 2011.
- Fassbender, A. J., Sabine, C. L., Feely, R. A., Langdon, C., and Mordy, C. W.: Inorganic carbon dynamics during northern California coastal upwelling, *Cont. Shelf Res.*, 31, 1180–1192, doi:10.1016/j.csr.2011.04.006, 2011.
- Feely, R. A., Sabine, C. L., Hernandez-Ayon, J. M., Ianson, D., and Hales, B.: Evidence for Upwelling of Corrosive “Acidified” Water onto the Continental Shelf., *Science*, 320, 1490–1492, doi:10.1126/science.1155676, 2008.
- Friederich, G., Walz, P., Burczynski, M., and Chavez, F. P.: Inorganic carbon in the central California upwelling system during the 1997–1999 El Niño–La Niña event, *Prog. Oceanogr.*, 54, 185–203, doi:10.1016/S0079-6611(02)00049-6, 2002.
- Gruber, N. and Sarmiento, J. L.: Biogeochemical/Physical Interactions in Elemental Cycles, in: *THE SEA: Biological-Physical Interactions in the Oceans*, edited by Robinson, A. R., McCarthy, J. J., and Rothschild, B., vol. 12, pp. 337–399, John Wiley and Sons, volume 12 Edn., 2002.
- Gruber, N., Frenzel, H., Doney, S. C., Marchesiello, P., McWilliams, J. C., Moisan, J. R., Oram, J. J., Plattner, G.-K., and Stolzenbach, K. D.: Eddy-resolving simulation of plankton ecosystem dynamics in the California Current System, *Deep-Sea Res. Pt. I*, 53, 1483–1516, 2006.
- Gruber, N., Gloor, M., Mikaloff Fletcher, S. E., Doney, S. C., Dutkiewicz, S., Follows, M. J., Gerber, M., Jacobson, A. R., Joos, F., Lindsay, K., Menemenlis, D., Mouchet, A., Müller, S. A., Sarmiento, J. L., and Takahashi, T.: Oceanic sources, sinks,

- and transport of atmospheric CO_2 , *Global Biogeochem. Cy.*, 23, GB1005, doi:10.1029/2008GB003349, 2009.
- Gruber, N., Lachkar, Z., Frenzel, H., Marchesiello, P., Münnich, M., McWilliams, J. C., Nagai, T., and Plattner, G.-K.: Eddy-induced reduction of biological production in eastern boundary upwelling systems, *Nature Geosci.*, 4, 787–792, 2011.
- Gruber, N., Hauri, C., Lachkar, Z., Loher, D., Frölicher, T. L., and Plattner, G.-K.: Rapid Progression of Ocean Acidification in the California Current System., *Science*, 337, 220–223, 2012.
- Hales, B., Takahashi, T., and Bandstra, L.: Atmospheric CO_2 uptake by a coastal upwelling system, *Global Biogeochem. Cy.*, 19, GB1009, doi:10.1029/2004GB002295, 2005.
- Hales, B., Strutton, P. G., Saraceno, M., Letelier, R., Takahashi, T., Feely, R. A., Sabine, C., and Chavez, F.: Satellite-based prediction of $p\text{CO}_2$ in coastal waters of the eastern North Pacific, *Prog. Oceanogr.*, 103, 1–15, 2012.
- Hauri, C., Gruber, N., Vogt, M., Doney, S. C., Feely, R. A., Lachkar, Z., Leinweber, A., McDonnell, A., Münnich, M., and Plattner, G.-K.: Spatiotemporal variability and long-term trends of ocean acidification in the California Current System, *Biogeosciences*, 10, 193–216, doi:10.5194/bg-10-193-2013, 2013.
- Jin, X., Gruber, N., Dunne, J. P., Sarmiento, J. L., and Armstrong, R. A.: Diagnosing the contribution of phytoplankton functional groups to the production and export of particulate organic carbon, CaCO_3 , and opal from global nutrient and alkalinity distributions, *Global Biogeochem. Cy.*, 20, GB2015, doi:10.1029/2005GB002532, 2006.
- Jones, S., Le Quéré, C., and Rödenbeck, C.: Autocorrelation characteristics of surface ocean $p\text{CO}_2$ and air–sea CO_2 fluxes, *Global Biogeochem. Cy.*, 26, GB2042, doi:10.1029/2010GB004017, 2012.
- Kahru, M., Kudela, R., Manzano-Sarabia, M., and Mitchell, B. G.: Trends in primary production in the California Current detected with satellite data, *J. Geophys. Res.*, 114, C02004, doi:10.1029/2008JC004979, 2009.
- Key, R. M., Kozyr, A., Sabine, C. L., Lee, K., Wanninkhof, R., Bullister, J. L., Feely, R. A., Millero, F. J., Mordy, C., and Peng, T.-H.: A global ocean carbon climatology: Results from Global Data Analysis Project (GLODAP), *Global Biogeochem. Cy.*, 18, GB4031, doi:10.1029/2004GB002247, 2004.
- Komhyr, W., Gammon, R., Harris, T., Waterman, L. S., Conway, T., Taylor, W., and Thoning, K.: Global Atmospheric Distribution and Variations From 1968–1982 NOAA/GMCC CO_2 Flask Sample Data, *J. Geophys. Res.*, 90, 5567–5596, 1985.
- Lachkar, Z. and Gruber, N.: What controls biological production in coastal upwelling systems? Insights from a comparative modeling study, *Biogeosciences*, 8, 2961–2976, doi:10.5194/bg-8-2961-2011, 2011.
- Lachkar, Z. and Gruber, N.: Response of biological production and air–sea CO_2 fluxes to upwelling intensification in the California and Canary Current Systems, *J. Mar. Syst.*, 109–110, 149–160, doi:10.1016/j.jmarsys.2012.04.003, 2013.
- Laruelle, G. G., Dürr, H. H., Slomp, C. P., and Borges, A. V.: Evaluation of sinks and sources of CO_2 in the global coastal ocean using a spatially-explicit typology of estuaries and continental shelves, *Geophys. Res. Lett.*, 37, L15607, doi:10.1029/2010GL043691, 2010.
- Lee, K.: Global net community production estimated from the annual cycle of surface water total dissolved inorganic carbon, *Limnology and Oceanography*, 46, 1287–1297, 2001.
- Lee, K., Tong, L. T., Millero, F. J., Sabine, C. L., Dickson, A. G., Goyet, C., Park, G.-H., Wanninkhof, R., Feely, R. A., and Key, R. M.: Global relationships of total alkalinity with salinity and temperature in surface waters of the world’s oceans, *Geophys. Res. Lett.*, 33, L19605, doi:10.1029/2006GL027207, 2006.
- Leinweber, A., Gruber, N., Frenzel, H., Friederich, G., and Chavez, F. P.: Diurnal carbon cycling in the surface ocean and lower atmosphere of Santa Monica Bay, California, *Geophys. Res. Lett.*, 36, L08601, doi:10.1029/2008GL037018, 2009.
- Liu, K.-K., Atkinson, L., Chen, C. A., Gao, S., Hall, J., MacDonald, R., Talaue-McManus, L., and Quiñones, R.: Exploring Continental Margin Carbon Fluxes on a Global Scale, *Eos Transactions, AGU*, 81, 641–644, 2000.
- Liu, K.-K., Atkinson, L., Quiñones, R., and Talaue-McManus, L.: Biogeochemistry of continental margins in a global context, in: *Carbon and Nutrient Fluxes in Continental Margins. Global Change – The IGBP Series*, edited by: Liu, K.-K., Atkinson, L., Quiñones, R., and Talaue-McManus, L., Springer Berlin Heidelberg, Berlin, 3–24, 2010.
- Lovenduski, N. S., Gruber, N., Doney, S. C., and Lima, I. D.: Enhanced CO_2 outgassing in the Southern Ocean from a positive phase of the Southern Annular Mode, *Global Biogeochem. Cy.*, 21, GB2026, doi:10.1029/2006GB002900, 2007.
- Marchesiello, P., McWilliams, J. C., and Shchepetkin, A.: Equilibrium structure and dynamics of the California Current System, *J. Phys. Oceanogr.*, 33, 753–783, 2003.
- Martiny, A. C., Pham, C. T., Primeau, F. W., Vrugt, J. A., Moore, J. K., Levin, S. A., and Lomas, M. W.: Strong latitudinal patterns in the elemental ratios of marine plankton and organic matter, *Nature Geosci.*, 6, 279–283, 2013.
- Mehrbach, C., Culbertson, C., Hawley, J., and Pytkowicz, R.: Measurement of the apparent dissociation constants of carbonic acid in seawater at atmospheric pressure, *Limnology and Oceanography*, 18, 897–907, 1973.
- Mikaloff Fletcher, S. E., Gruber, N., Jacobson, A. R., Doney, S. C., Dutkiewicz, S., Gerber, M., Follows, M., Joos, F., Lindsay, K., Menemenlis, D., Mouchet, A., Müller, S. A., and Sarmiento, J. L.: Inverse estimates of anthropogenic CO_2 uptake, transport, and storage by the ocean, *Global Biogeochem. Cy.*, 20, GB2002, doi:10.1029/2005GB002530, 2006.
- Millero, F. J.: Thermodynamics of the carbon dioxide system in the oceans, *Geochimica et Cosmochimica Acta*, 59, 661–677, doi:10.1016/0016-7037(94)00354-O, 1995.
- Muller-Karger, F. E., Varela, R., Thunell, R., Luerssen, R., Hu, C., and Walsh, J. J.: The importance of continental margins in the global carbon cycle, *Geophys. Res. Lett.*, 32, L01602, doi:10.1029/2004GL021346, 2005.
- Murnane, R., Sarmiento, J. L., and Le Quéré, C.: Spatial distribution of air–sea CO_2 fluxes and the interhemispheric transport of carbon by the oceans, *Global Biogeochem. Cy.*, 13, 287–305, 1999.
- Nagai, T., Gruber, N., Frenzel, H., McWilliams, J. C., and Plattner, G.-K.: Dominant role of eddies in offshore transport in the California Current System, in preparation, 2014.
- Pennington, J., Castro, C., Collins, C., Evans, W., Friederich, G., Michisaki, R., and Chavez, F.: The Northern and Central California Coastal Upwelling System, in: *Carbon and Nutrient*

- Fluxes in Continental Margins, Global Change The IGBP Series, edited by: Liu, K.-K., Atkinson, L., Quiñones, R., and Talaue-McManus, L., Springer Berlin Heidelberg, 29–44, 2010.
- Pfeil, B., Olsen, A., Bakker, D. C. E., Hankin, S., Koyuk, H., Kozyr, A., Malczyk, J., Manke, A., Metzl, N., Sabine, C. L., Akl, J., Alin, S. R., Bates, N., Bellerby, R. G. J., Borges, A., Boutin, J., Brown, P. J., Cai, W.-J., Chavez, F. P., Chen, A., Cosca, C., Fassbender, A. J., Feely, R. A., González-Dávila, M., Goyet, C., Hales, B., Hardman-Mountford, N., Heinze, C., Hood, M., Hoppema, M., Hunt, C. W., Hydes, D., Ishii, M., Johannessen, T., Jones, S. D., Key, R. M., Körtzinger, A., Landschützer, P., Lauvset, S. K., Lefèvre, N., Lenton, A., Lourantou, A., Merlivat, L., Midorikawa, T., Mintrop, L., Miyazaki, C., Murata, A., Nakadate, A., Nakano, Y., Nakaoka, S., Nojiri, Y., Omar, A. M., Padin, X. A., Park, G.-H., Paterson, K., Perez, F. F., Pierrot, D., Poisson, A., Ríos, A. F., Santana-Casiano, J. M., Salisbury, J., Sarma, V. V. S. S., Schlitzer, R., Schneider, B., Schuster, U., Sieger, R., Skjelvan, I., Steinhoff, T., Suzuki, T., Takahashi, T., Tedesco, K., Telszewski, M., Thomas, H., Tilbrook, B., Tjiputra, J., Vandemark, D., Veness, T., Wanninkhof, R., Watson, A. J., Weiss, R., Wong, C. S., and Yoshikawa-Inoue, H.: A uniform, quality controlled Surface Ocean CO_2 Atlas (SOCAT), *Earth Syst. Sci. Data*, 5, 125–143, 2013, <http://www.earth-syst-sci-data.net/5/125/2013/>.
- Plattner, G.-K., Gruber, N., Frenzel, H., and McWilliams, J. C.: Decoupling marine export production from new production, *Geophys. Res. Lett.*, 32, L11612, doi:10.1029/2005GL022660, 2005.
- Redfield, A., Ketchum, B., and Richards, F.: The influence of organisms on the composition of seawater, in: *THE SEA: Ideas and Observations on Progress in the Study of the Sea*, edited by: Hill, M., Wiley Interscience, New York, USA, 26–77, 1963.
- Regnier, P., Friedlingstein, P., Ciais, P., Mackenzie, F. T., Gruber, N., Janssens, I. A., Laruelle, G. G., Lauerwald, R., Luysaert, S., Andersson, A. J., Arndt, S., Arnosti, C., Borges, A. V., Dale, A. W., Gallego-Sala, A., Goddérís, Y., Goossens, N., Hartmann, J., Heinze, C., Ilyina, T., Joos, F., LaRowe, D. E., Leifeld, J., Meysman, F. J. R., Munhoven, G., Raymond, P. A., Spahni, R., Suntharalingam, P., and Thullner, M.: Anthropogenic perturbation of the carbon fluxes from land to ocean, *Nature Geosci.*, 6, 597–607, 2013.
- Sarmiento, J. L. and Gruber, N.: *Ocean Biogeochemical Dynamics*, Princeton University Press, Princeton, New Jersey, USA, 2006.
- Sarmiento, J. L., Dunne, J., Gnanadesikan, A., Key, R. M., Matsumoto, K., and Slater, R.: A new estimate of the CaCO_3 to organic carbon export ratio, *Global Biogeochem. Cy.*, 16, 1107, doi:10.1029/2002GB001919, 2002.
- Schmittner, A., Gruber, N., Mix, A., Key, R., Tagliabue, A., and Westberry, T.: Biology and air–sea gas exchange controls on the distribution of carbon isotope ratios ($\delta^{13}\text{C}$) in the ocean, *Biogeosciences*, 10, 5793–5816, doi:10.5194/bg-10-5793-2013, 2013.
- Shchepetkin, A. F. and McWilliams, J. C.: The regional oceanic modeling system (ROMS): a split-explicit, free-surface, topography-following-coordinate oceanic model, *Ocean Modell.*, 9, 347–404, 2005.
- Takahashi, T., Sutherland, S. C., Feely, R. A., and Wanninkhof, R.: Decadal change of the surface water $p\text{CO}_2$ in the North Pacific: A synthesis of 35 years of observations, *J. Geophys. Res.*, 111, C07S05, doi:10.1029/2005JC003074, 2006.
- Takahashi, T., Sutherland, S. C., Wanninkhof, R., Sweeney, C., Feely, R. A., Chipman, D. W., Hales, B., Friederich, G., Chavez, F., Sabine, C., Watson, A., Bakker, D. C., Schuster, U., Metzl, N., Yoshikawa-Inoue, H., Ishii, M., Midorikawa, T., Nojiri, Y., Körtzinger, A., Steinhoff, T., Hoppema, M., Olafsson, J., Arnarson, T. S., Tilbrook, B., Johannessen, T., Olsen, A., Bellerby, R., Wong, C., Delille, B., Bates, N., and de Baar, H. J.: Climatological mean and decadal change in surface ocean $p\text{CO}_2$, and net sea–air CO_2 flux over the global oceans, *Deep-Sea Res. Pt. II*, 56, 554–577, 2009.
- Takahashi, T., Sutherland, S., and Kozyr, A.: Global ocean surface water partial pressure of CO_2 database: Measurements performed during 1957–2012 (Version 2012). ORNL/CDIAC-160, NDP-088(V2012), Carbon Dioxide Information Analysis Center, Oak Ridge National Laboratory, U.S. Department of Energy, Oak Ridge, Tennessee, doi:10.3334/CDIAC/OTG.NDP088(V2012), 2013.
- Taylor, K. E.: Summarizing multiple aspects of model performance in a single diagram, *J. Geophys. Res.*, 106, 7183–7192, doi:10.1029/2000JD900719, 2001.
- Toggweiler, J. R., Murnane, R., Carson, S., Gnanadesikan, A., and Sarmiento, J. L.: Representation of the carbon cycle in box models and GCMs, 2. Organic pump, *Global Biogeochem. Cy.*, 17, 1027, doi:10.1029/2001GB001841, 2003.
- Volk, T. and Hoffert, M. I.: Ocean carbon pumps: Analysis of relative strengths and efficiencies in ocean-driven atmospheric CO_2 changes, in: *The Carbon Cycle and Atmospheric CO_2 : Natural Variations Archean to Present*, Geophysical Monograph Series, edited by: Sundquist, E. T. and Broecker, W. S., vol. 32, Washington, DC, doi:10.1029/GM032p0099, 99–110, 1985.
- Wanninkhof, R.: Relationship Between Wind Speed and Gas Exchange Over the Ocean, *J. Geophys. Res.*, 97, 7373–7382, 1992.
- Wanninkhof, R., Park, G. H., Takahashi, T., Sweeney, C., Feely, R., Nojiri, Y., Gruber, N., Doney, S. C., McKinley, G. A., Lenton, A., Le Quéré, C., Heinze, C., Schwinger, J., Graven, H., and Khatiwala, S.: Global ocean carbon uptake: magnitude, variability and trends, *Biogeosciences*, 10, 1983–2000, doi:10.5194/bg-10-1983-2013, 2013.
- Weiss, R. F.: Carbon dioxide in water and seawater: the solubility of a non-ideal gas, *Mar. Chem.*, 2, 203–215, doi:10.1016/0304-4203(74)90015-2, 1974.